

1 **Near real-time atmospheric and oceanic science products of Himawari-8/9**
2 **geostationary satellites over the South China Sea**

3
4 Jian Liu¹, Jingjing Yu¹, Chuyong Lin¹, Min He¹, Haiyan Liu¹, Wei Wang², Min Min^{2*}
5

6
7 ¹ School of Geography and Ocean Science, Ministry of Education Key Laboratory for Coast
8 and Island Development, Nanjing University, Nanjing 210023, China, and Southern Marine
9 Science and Engineering Guangdong Laboratory (Zhuhai), Zhuhai 519082, China

10 ² School of Atmospheric Sciences and Guangdong Province Key Laboratory for Climate
11 Change and Natural Disaster Studies, Sun Yat-sen University, Zhuhai 519082, China

12
13
14
15
16
17
18 *Corresponding author: minm5@mail.sysu.edu.cn
19
20
21
22
23
24
25
26

27
28
29
30
31
32
33
34
35
36
37
38
39
40
41
42
43
44
45
46
47
48
49
50
51
52
53
54
55
56

Abstract

The initial release of near real-time (NRT) atmospheric and oceanic science products from Japanese Himawari-8/9 (H8/9) geostationary (GEO) satellites over the South China Sea (SCS) was unveiled in 2024. The primary objective behind crafting these NRT H8/9 satellite products is to facilitate weather and marine environment monitoring, enhance maritime security, and aid ocean navigation, among other purposes. As part of this investigation, a novel NRT data processing system was devised to generate a variety of regional H8/9 GEO satellite science products within a resolution of 10 minutes and a gridded resolution of $0.05^\circ \times 0.05^\circ$ from November 3, 2022 to the present. This algorithm system was built upon the preceding FengYun (FY) geostationary satellite algorithm testbed (FYGAT), which was the prototype of FY-4 GEO meteorological satellite science product operational processing system. These regional H8/9 GEO satellite science products encompass a range of crucial data such as cloud mask, fraction, height, phase, optical and microphysical properties, layered precipitable water, sea surface temperature, etc. We subjected these products to rigorous evaluations against high-quality analogous satellite products and reanalysis data spanning [one year](#) in 2023. The validations underscore a strong consistency between the H8/9 GEO satellite atmospheric and oceanic science products over the SCS and the referenced products. Nevertheless, slight discrepancies in these satellite science products were identified, primarily stemming from variations in sensor/dataset characteristics, retrieval algorithms, and geometric conditions. These outcomes demonstrate the suitability of the first edition of NRT atmospheric and oceanic science products of H8/9 satellites over the SCS in supporting the intended quantitative applications. This NRT GEO satellite data record is publicly accessible through the File Transfer Protocol (FTP) provided by the Southern Marine Science and Engineering Guangdong Laboratory (Zhuhai) in China. Free access to the dataset can be found at <https://doi.org/10.6084/m9.figshare.25015853> (Liu Jian, 2024).

Keywords: Cloud; Geostationary Satellite; South China Sea; Layered Precipitable Water; Sea surface temperature.

删除了: temporal

删除了: four months

59 **1 Introduction**

60 The South China Sea is located to the south of mainland China and in the western
61 Pacific Ocean. It stands as the largest and deepest sea area in China, with an average
62 depth of 1212 meters and reaching a maximum depth of 5559 meters. Due to its
63 proximity to the equator, the SCS receives a substantial amount of solar radiation,
64 resulting in high local temperatures and humidity. The regional annual average air
65 temperature ranges from 298.15 K to 301.15 K. Even during the coldest months, the
66 average temperatures remain above 293.15 K, while extreme high-temperature events
67 can reach about 306.15 K. The average sea surface temperature (SST) in the SCS is
68 around 299.15 K, and the seasonal variation is not significant. Furthermore, the South
69 China Sea and the Western Pacific serve as abundant sources of water vapor, leading
70 to considerable precipitation in the SCS. Typhoon-related rainfall accounts for about
71 one-third of the total rainfall in the region. On average, the SCS experiences over 1300
72 mm of rainfall annually, with the majority concentrated in the summer half-year (Wang
73 et al., 2011; Wang et al., 2009; Ding and Liu, 2001).

74 The SCS region experiences a distinct tropical maritime monsoon climate.
75 Beginning in October each year, winter air currents originating from Siberia and the
76 Mongolian Plateau consistently flow toward the SCS (Martin and Howland, 1982). As
77 a result, from November to March of the following year, the SCS region is dominated
78 by the northeast monsoon. Starting in April, the SCS is influenced by tropical and
79 equatorial ocean air masses, inducing the prevalence of the southwest monsoon from
80 May to September. Additionally, the SCS is often affected by typhoons during the
81 summer and autumn seasons. About 70% of these typhoons originate from the Western
82 Pacific, east of the Philippines, and the vicinity of the Caroline Islands, while the
83 remaining 30% are generated locally in the sea areas near the Xisha and Zhongsha
84 Islands in the SCS (Ding and Liu, 2001; Wang et al., 2020; Niu and Feng, 2021; Jiang
85 et al., 2023).

86 Due to the lack of ground-based observations over the SCS, satellites, particularly
87 geostationary (GEO) meteorological satellites, have become the most effective means
88 of observing weather patterns, climate, and environmental changes in oceanic regions.
89 For instance, satellite-based rain rate, SST, outgoing longwave radiation (ORL), and
90 convective clouds, etc. are commonly used to identify the summer monsoon, marine
91 heatwave, rainfall, and convection over the SCS (Liu et al., 2014; Xu et al., 2021; Li et
92 al., 2022b; Koseki et al., 2013; Zhou et al., 2024). In recent years, countries across the

删除了: boasting

删除了: 25°C

删除了: 28°C

删除了: 20°C

删除了: 33°C

删除了: 26°C

删除了: also

删除了: After

删除了: of

删除了: s

删除了: Besides

删除了: from

删除了: On account of

删除了: emerged as

删除了: for

删除了: examine

109 world, such as China, U.S., Japan, and Korea, have made their own remarkable progress
110 in the development of next-generation geostationary meteorological satellites.
111 Enhanced imaging capabilities in spectral, temporal, and spatial resolutions of the next-
112 generation GEO meteorological satellite allows for more detailed and accurate
113 observations of cloud formations, atmospheric conditions, and natural disasters like
114 hurricanes and typhoons, such as Fengyun-4A/B (FY-4) operated by the China
115 Meteorological Administration (CMA) and Himawari-8/9 (H8/9) satellites operated by
116 the Japan Meteorological Agency (JMA) (Yang et al., 2017; Schmit et al., 2017; Husi
117 et al., 2019; Kim et al., 2021). ~~In additional to~~ GEO advanced imager, many nations
118 have equipped their geostationary lightning and infrared hyperspectral sound~~ing~~
119 detection sensors to track and analyze thunderstorms, lightning activities, atmospheric
120 temperature and humidity profiles, and even wind fields in real-time (Min et al., 2017b;
121 Ma et al., 2021; Li et al., 2022a).

122 Although the JAXA (Japan Aerospace Exploration Agency) official FTP site
123 (ftp.ptree.jaxa.jp) has already offered the freely download links ~~for~~ some H8/9 Level-2
124 (L2) science products, such as cloud phase and optical depth (Husi et al., 2019), from
125 July 7 of 2015, ~~to the~~ present with approximate two hours lag, the relatively low
126 timeliness and lack of variety of operational satellite science products have seriously
127 affected the data quantitative applications in weather and marine environment
128 monitoring over the SCS. Particularly, time-delayed GEO satellite products cannot be
129 utilized in maritime security and navigation fields, which are of vital importance as it
130 ensures the safety of crew members, transportation of goods, protection of the marine
131 environment, etc. (Soldi et al., 2021). However, as recommended by the JMA, the near
132 real-time down-sampling full-disk H8/9 Level-1B (L1B) radiance data (including 14
133 bands with horizontal resolutions of 1 km (visible, VIS) and 4 km (near infrared and
134 infrared, NIR and IR bands), and excluding two VIS bands at 0.47 μm and 0.51 μm)
135 are able to be received by using the compact and exclusive geostationary satellite data
136 receiving antenna from the JMA Himawari-Cast (Xia et al., 2023; Wang et al., 2019).
137 Therefore, based on the received real-time H8/9 full-disk L1B data, the primary goal of
138 this investigation is to develop several NRT L2 Atmospheric aNd Oceanic science
139 products over the SCS (abbreviated as NANO_SCS) that are released online. It is the
140 first edition of the NRT H8/9 GEO satellite science products generated by the
141 NANO_SCS system. The next sections will be devoted to the introduction and
142 validation of these NRT H8/9 GEO satellite scientific products. Both the NANO_SCS

删除了: Expect to

删除了: er

删除了: y

删除了: of

147 satellite data processing and management systems are operated by the Southern Marine
148 Science and Engineering Guangdong Laboratory (Zhuhai) of China.

149 The subsequent sections of this study are meticulously organized as follows.
150 Section 2 briefly introduces the Himawari-8/9 satellites, elucidating the intricate details
151 of the main processing or production flow, as well as shedding light on the remarkable
152 NRT science products specifically tailored for the South China Sea region. Section 3
153 shows some sample results and verification of key science products, in terms of
154 accuracy and reliability. Section 4 elucidates data download method. Finally, in Section
155 5, we summarize the main conclusions of this study, while also outlining our future
156 vision plans for further enhancing and expanding the scope of the NANO_SCS dataset.
157

158 2 Data production

159 2.1 Data

160 The Himawari-8/9 satellites, which are the new-generation and state-of-the-art GEO
161 meteorological satellites operated by the JMA, were successfully launched on October
162 7, 2014, and November 2, 2016, respectively. These advanced satellites operate in a
163 highly sophisticated three-axis stabilized mode, ensuring high spatial-temporal, precise
164 and stable observations. It is worth highlighting that on December 13, 2022, at 05:00
165 UTC, the H9 GEO meteorological satellite seamlessly replaced its predecessor, the H8
166 GEO satellite, marking a significant milestone in GEO satellite operations
167 (<https://www.data.jma.go.jp/mscweb/en/index.html>). This strategic location allows for
168 comprehensive full-disk observation mode, enabling the satellites to capture detailed
169 imagery of the entire Earth's disk, with a particular focus on the Japanese island and its
170 surrounding areas. The Advanced Himawari Imager (AHI), as a unique and highly
171 advanced optical sensor designed specifically for earth viewing, has 16 independent
172 earth-view bands, covering an extensive range of wavelengths from 0.45 to 13.3 μm .
173 These bands include three visible (VIS) bands, three near-infrared (NIR) bands, and ten
174 infrared (IR) bands, each serving a specific purpose in capturing and analyzing various
175 aspects of the Earth's atmosphere and surface. The AHI routinely operates in two
176 observation modes: a full-disk observation mode that captures full disk images within
177 a 10-minute time interval, and a fast regional scanning mode that allows for swift
178 maneuvering and scanning within a 2.5-minute interval. This regional scanning mode
179 is particularly useful for capturing high-resolution imagery of specific regions of

删除了: In

删除了: , it

删除了: verifies

删除了: the

删除了: , ensuring their

185 interest, enabling detailed analysis and examination of localized weather events. The
186 nominal spatial resolutions of the H8/9-AHI sensor vary depending on the specific band
187 being utilized. For the VIS band at 0.65 μm , the spatial resolution is 0.5 km. The NIR
188 bands have a spatial resolution of 1 km, while the IR bands have a spatial resolution of
189 2 km (Husi et al., 2019; Bessho et al., 2016; Letu et al., 2020; Min et al., 2019). In this
190 study, we only used the down-sampling H8/9 L1B radiance data mentioned before to
191 ~~produce~~ NRT dataset. The spatial resolution for the down-sampling VIS band at 0.65
192 μm was reduced to 1.0 km, while the other bands were down-sampled to 4.0 km. The
193 scope of this investigation covers the South China Sea region, specifically from 0° to
194 40°N latitude and 100°E to 140°E longitude. The utilization of IR bands with a spatial
195 resolution of 4.0 km limits the related L2 satellite science products to the same
196 resolution. Therefore, based on the products with the spatial resolution of 4.0 km, the
197 final regional L2 atmospheric and oceanic science products are analyzed and projected
198 into a user-friendly gridded resolution of $0.05^\circ \times 0.05^\circ$.

199 The NRT GEO satellite retrieval system (or NANO_SCS system) developed in this
200 study also utilizes the high-resolution operational numerical weather prediction (NWP)
201 data from Global Forecast System (GFS) ~~as ancillary data~~, which ~~has~~ a gridded
202 horizontal resolution of $0.25^\circ \times 0.25^\circ$ and encompasses a 41 vertical layers ranging
203 from 1000 to 0.01 hPa within a 3-hour time interval. The GFS NWP data can be
204 effortlessly accessed and downloaded from the National Oceanic and Atmospheric
205 Administration (NOAA) website
206 (<https://nomads.ncep.noaa.gov/pub/data/nccf/com/gfs/prod>) at four distinct initial
207 forecast times (00_00, 06_00, 12_00, and 18_00 UTC). To ensure optimal efficiency
208 for the operations of subsequent day, only 9 continuous data (ranging from 018, 021,
209 024, ... to 042) generated at a fixed initial forecast time of UTC 06_00 are selectively
210 downloaded within a predefined time period each day (Whitaker et al., 2008).

211 We collect and use ~~one year~~ (2023) ~~of~~ Climate Data Records (CDR) from the latest
212 MODIS (Moderate Resolution Imaging Spectroradiometer) Collection-6.1 Level-2
213 cloud, land surface temperature (LST), and sea surface temperature (SST) products to
214 validate the NRT H8/9 GEO satellite science products (Platnick et al., 2003; Platnick
215 et al., 2017). MODIS, as a key optical sensor aboard NASA's Terra and Aqua polar-
216 orbiting satellites since 1999 and 2002 (~~respectively~~), can provide high resolution (1.0
217 km) L2 science products about the Earth's surface and atmosphere
218 (<https://search.earthdata.nasa.gov/search>). MODIS data are freely available to the

删除了: product

删除了: as ancillary data

删除了: the

删除了: boast

删除了: four months

删除了: January, April, July, and October of

删除了:

226 public and are widely used by scientists, government agencies, and researchers around
227 the world, which are often used to verify the other congeneric satellite products (Min
228 et al., 2020). Furthermore, we also compare the NRT layered precipitable water (LPW)
229 product over the SCS with matched ERA5 reanalysis data (the fifth-generation
230 European Center for Medium Range Weather Forecasts Reanalysis data) (Hersbach et
231 al., 2020). The hourly layered specific humidity data for the same year (2023), with a
232 horizontal resolution of $0.25^{\circ} \times 0.25^{\circ}$ have been downloaded freely from the ERA5
233 dataset. This data will be employed for the validation of the layered precipitable water
234 product of H8/9 GEO satellite. You can access the data at
235 <https://cds.climate.copernicus.eu/cdsapp#!/home>.

删除了: always

删除了: four months (January, April, July, and October of 2023)...

236

237 *2.2 NRT processing flow and science products*

238 As extensively discussed in the former study by (Min et al., 2017b), significant strides
239 were made in the development of the operational prototypes of FY-4 GEO satellite
240 science product algorithms. These remarkable advancements were achieved through
241 the collaborative efforts of the scientists in the FY-4 GEO satellite Algorithm Working
242 Group (AWG) in China, who successfully developed two highly robust Fengyun
243 science product algorithm testbeds (or FYGAT) specifically tailored for imagers and
244 sounders. For a comprehensive understanding of the intricate details of FYGAT,
245 interested readers are strongly encouraged to refer to the aforementioned literature
246 written by (Min et al., 2017b). The FYGAT for imager is the key module of the
247 NANO_SCS system for rapidly retrieving the first edition of NRT L2 science products
248 of H8/9 GEO satellites.

删除了: retrieve

249 Figure 1 shows the comprehensive NRT processing flowchart of the NANO_SCS
250 system. The dark gray shading cylinder icons in the figure represent the key processing
251 modules of the system, including retrieval, projection, and drawing modules. Following
252 the synthesis of NRT satellite data, the retrieval module initially retrieves the cloud
253 mask product to identify clear and cloudy-sky pixels within the targeted SCS region.
254 Then, for cloudy-sky pixels, the retrieval module sequentially executes algorithms for
255 retrieving cloud fraction, cloud type/phase, cloud top properties, cloud optical and
256 microphysical properties, and cloud base properties products. However, the accurate
257 retrieval of science products from previous algorithms is crucial for the successful
258 execution of subsequent backend algorithms. For instance, the cloud optical and
259 microphysical properties algorithm relies on inputs such as cloud phase and top

删除了:

265 properties to determine specific ice/water cloud optical and radiative properties lookup
266 tables (LUT) and atmospheric correction methods above the cloud (Platnick et al., 2017;
267 Walther et al., 2011) used in retrieval procedure. In a stark contrast, other science
268 algorithms for clear-sky pixels can be executed in parallel as they are independent of
269 each other, such as the algorithms for land surface temperature (LST) and sea surface
270 temperature (SST). It is important to note that due to retrieval efficiency and computing
271 resource limitations, the physics-based layered precipitable water (LPW) algorithm
272 (Zhu et al., 2023) is executed only once every half an hour.

273 Table 1 provides a list of the main NRT H8/9 GEO satellite atmospheric and oceanic
274 science products in the first edition, along with their corresponding variables, generated
275 by the NANO_SCS system from 3 November 2022 to the present. It includes the
276 variable name, valid value, and corresponding notes of satellite science products. These
277 products are stored in the Hierarchical Data Format-5 (HDF5) format within a 10-
278 minute interval. The NRT GEO satellite science product is typically referred to as
279 "AH19_L2_CLM_20230815_0650_4000M_proj.hdf5". In this naming convention, the
280 abbreviation of "CLM" stands for Cloud Mask (all abbreviations are three characters
281 long), while "20230815_0650" denotes the specific observation time of the satellite
282 data, including year, month, day, hour, and minute. Lastly, "4000M_proj" indicates the
283 spatial resolution of 4000 meters and projected data. Certain related variables, such as
284 cloud top temperature, pressure, and height, are stored in the same HDF5 format GEO
285 satellite science product file, specifically the CTP (Cloud Top Properties) product file
286 (refer to Table 1).

287 Figure 2 displays the quick view images of cloud top height, cloud mask, cloud base
288 height, and cloud optical depth at 03:00 UTC on July 31, 2023, as well as atmospheric
289 total precipitable water (from LPW product) and SST retrieved at clear-sky pixels at
290 10:00 UTC on August 15, 2023, over the SCS. These NRT product images are obtained
291 from the NANO_SCS system. The four cloud product subfigures from July 31, 2023,
292 capture the presence of Super Typhoon "Khanun" (its international number: 2306),
293 which originated in the southwestern waters of Guam on July 22, 2023. It has been
294 observed that the cloud system of Super Typhoon "Khanun" can reach maximum cloud
295 top heights exceeding 16 km and minimum cloud base height lower than 1 km. The
296 productions of all the NRT satellite science products and quick view images of the
297 NANO_SCS system are typically delayed by approximately 17 minutes from the
298 observation time. Besides, a user-friendly quick-view website

删除了: HDF5

300 (<http://meteorsatellite.hellosea.org.cn/#/index>) has been created to provide users with a
301 convenient way to access and monitor the NRT H8/9 satellite data over the SCS.

302

303 **3. Results and validations**

304 *3.1 Cloud mask and fraction*

305 To differentiate between clear-sky and cloudy pixels in satellite earth-view image,
306 the cloud mask (CLM) product is firstly retrieved by the NANO_SCS system (refer to
307 Figure 1). ~~This~~ serves as a fundamental and primary L2 scientific output of GEO
308 satellite imaging sensors, playing a crucial role in generating high-quality subsequent
309 satellite products. As mentioned in the previous studies (Liang et al., 2023; Wang et al.,
310 2019; Heidinger et al., 2012), we used the new unified cloud mask algorithm (Wang et
311 al., 2019) of early development to retrieve and generate H8/9 CLM product firstly.
312 Utilizing the 0.64, 1.61, 3.88, 7.3, 11.2, and 12.3 μm channels of H8/9-AHI, the CLM
313 algorithm on this GEO satellite will perform 13 distinct cloud/clear-sky tests. These
314 tests are categorized into four groups: solar reflectance (SolRef), infrared (IR),
315 shortwave infrared (SWIR), and spatial uniformity tests (Wang et al., 2019; Xia et al.,
316 2024).

317 After successfully retrieving the cloud mask product, similar to the MODIS
318 algorithm (Zhao and Girolamo, 2006), cloud fraction (CLF) is calculated in a down-
319 sampled 5×5 neighboring pixel box as follows:

$$320 \text{Cloud Fraction} = 100\% \times (A + B) / (5 \times 5), \quad (1)$$

321 where A and B represent the total numbers of cloudy and probably cloudy pixels in the
322 same 5×5 neighboring pixel box, respectively. It is noting that the cloud fraction
323 product is also projected into a user-friendly gridded resolution of $0.05^\circ \times 0.05^\circ$. More
324 descriptions on these two products can be found in Table 1.

325 A pixel-to-pixel validation was performed on the H8/9 satellite CLM product over
326 the SCS using [one year](#) of MODIS data from the NANO_SCS system. To quantitatively
327 assess the quality of the GEO satellite CLM product, we employed four significant
328 scores: the probability of detection (POD) or recall rate, the false-alarm ratio (FAR),
329 the hit rate (HR) or accuracy, and the Kuiper's skill score (KSS). These metrics were
330 divided into PODcld, PODclr, FARcld, and FARclr, indicating clear and cloudy pixels
331 respectively. For detailed equations and meanings, please refer to previous literature
332 (Wang et al., 2019). In Figure 3a~3d, we present two cloud mask comparison samples
333 between H9/AHI GEO satellite and MODIS at 05:10 and 17:20 UTC on January 8,

删除了: It

删除了: four months

336 2023. It is evident that the CLM results from H9/AHI align well with the latest MODIS
 337 official products across both land and sea. Additionally, Figure 3e displays the POD,
 338 FAR, HR, and KSS scores of H9/AHI results for all matched pixels over land and ocean.
 339 Notably, both POD_{cl} and HR exceed 0.90, consistent with our prior study (Wang et
 340 al., 2019), indicating a relatively high-quality CLM product. Moreover, considering
 341 that cloud fraction depends on the cloud mask product (refer to Eq. (1)), we opted
 342 against using similar products for verification in this analysis.

343

344 3.2 Cloud type and phase

345 Cloud type and phase as thermodynamics characteristics signify the state of water
 346 vapor and minuscule particles within the cloud. It plays a critical role in weather and
 347 climate research as different cloud phases influence the reflection and absorption of
 348 solar radiation, consequently impacting Earth's energy balance and climate change
 349 (Mülmenstädt et al., 2021). Due to the similarities in detection channels (using 7.3, 8.5,
 350 11.2, and 12.3 μm channels), the cloud type and phase (CLP) retrieval algorithm
 351 developed here for H8/9-AHI was based on the corresponding algorithm used for U.S.
 352 new-generation Geostationary Operational Environmental Satellites (GOES-R)
 353 (Pavolonis et al., 2005; Pavolonis, 2010b). The physical foundation of this algorithm is
 354 the radiative transfer equation or forward model for cloudy sky at a specific infrared
 355 wavelength λ , which can be expressed as follows (Min et al., 2020):

$$356 I_{obs}(\lambda) = \varepsilon(\lambda)I_{ac}(\lambda) + \varepsilon(\lambda)T_{ac}(\lambda)B(\lambda, t_{eff}) + I_{clr}(\lambda)[1 - \varepsilon(\lambda)], \quad (2)$$

357 where I_{obs} is the observed radiance, I_{clr} is the clear-sky radiance, and I_{ac} is the above-
 358 cloud upwelling atmospheric radiance, respectively. I_{clr} can be precisely simulated by
 359 the coupled fast IR radiative transfer model in the FYGAT system with the input of
 360 matched GFS NWP data. ε and T_{ac} respectively represent the cloud emissivity and
 361 above-cloud transmittance. B and t_{eff} are the Planck function and the cloud effective
 362 temperature, respectively.

363 From Eq. (2), a pair of effective cloud emissivity from two different channels can be
 364 used to calculate the ratio of effective absorption optical thickness τ_{abs} of cloud, which
 365 is known as the beta ratio (β) and written as follows (Heidinger and Pavolonis, 2009;
 366 Parol et al., 1991):

$$367 \beta_{obs} = \frac{\ln[1-\varepsilon(\lambda_1)]}{\ln[1-\varepsilon(\lambda_2)]} = \frac{\tau_{abs}(\lambda_1)}{\tau_{abs}(\lambda_2)}, \quad (3)$$

删除了:

369 Actually, this parameter represents the ratio of the effective absorption optical depth at
370 two different channels or wavelengths. It can describe β_{obs} by utilizing the computed
371 single scattering properties of cloud particles, along with a given cloud particle size
372 distribution and optical properties. (Parol et al., 1991). The β_{theory} can be expressed as
373 follows:

$$374 \beta_{theory} = \frac{[1-\omega(\lambda_1)g(\lambda_1)]\alpha_{ext}(\lambda_1)}{[1-\omega(\lambda_2)g(\lambda_2)]\alpha_{ext}(\lambda_2)}, \quad (4)$$

375 where ω , g , and α_{ext} are the single scattering albedo, asymmetry parameter, and
376 extinction cross section, respectively. Considering the weak impact of multiple
377 scattering, Parol et al., (1991) demonstrated a good approximation of $\beta_{theory} \approx \beta_{obs}$ in the
378 range of 8~15 μm . Eq. (4) is independent of satellite observed radiance, cloud altitude,
379 or cloud optical thickness. By using β ratio instead of brightness temperature difference
380 (BTD), it not only considers the contribution of clear-sky conditions to radiation but
381 also provides a method to link observations with theoretical cloud particle distribution
382 and optical properties.

383 Based on the differences in β ratios (i.e. $\beta[8.5/11.2\mu\text{m}]$, $\beta[12.3/11.2\mu\text{m}]$, and
384 $\beta[7.3/11.2\mu\text{m}]$) between ice and water clouds, this algorithm effectively identifies cloud
385 type and phase by integrating cloud emissivity ϵ with observed brightness temperature.
386 More details of this algorithm can be found from the previous literatures (Pavolonis,
387 2010a; Pavolonis, 2010b). The six specific cloud types of this CLP product include
388 liquid water (cloud top temperature > 273K), supercooled water (liquid water clouds
389 with cloud top temperature < 273K), mixed (which encompass both ice and water
390 clouds), optically thick ice, optically thin ice, and multilayered ice clouds. The cloud
391 phase product can be defined by summarizing the first three types of clouds and ice
392 phase clouds using the last three different ice clouds (see Table 1).

393 Figure 4 illustrates the cloud phase comparisons between the H9/AHI GEO satellite
394 and MODIS at 05:10 UTC on January 8, 2023, and 04:30 UTC on July 10, 2023. This
395 comparison reveals consistent results between the two products. Notably, in Figures 4a
396 and 4c, the new H9/AHI cloud phase product identifies some newly added mixed-phase
397 cloud targets, a feature lacking in the MODIS official cloud phase product (King et al.,
398 1997). However, despite this addition, the distribution pattern of cloud phases remains
399 consistent between the two products as depicted in Figure 4. The POD and FAR for ice
400 and water clouds (Lai et al., 2019) are 0.94/0.17 and 0.68/0.14, respectively.

401

删除了: i

删除了: the

删除了:)

删除了: 5

删除了: 70

删除了: 3

408 3.3 Cloud top and base properties

409 Cloud geometry thickness (CGT), including top and base heights (CTP and CBP),
410 enables the profiling of the vertical structure of clouds, which is vital for understanding
411 global weather and climate systems (Viúdez-Mora et al., 2015; Wang et al., 2022).
412 Using the same beta ratio (β) theory discussed in Section 3.2, the optimal estimation
413 (OE) method (Rodgers, 2000), and observed brightness temperatures (BT) at 11.2, 12.3,
414 and 13.3 μm channels, a classical one-dimensional variational (1DVAR) algorithm
415 applies a cost function ζ (refer to Eq. 5) to estimate the cloud top temperature (CTT),
416 which can be written as follows :

$$417 \zeta = [x - x_a]^T Cov_a^{-1} [x - x_a] + [y - M(x)]^T Cov_y^{-1} [y - M(x)], \quad (5)$$

418 where x , y , x_a , $M(x)$, Cov_a , and Cov_y , represent the posterior state vectors, the
419 observation vectors (include $BT_{11\mu\text{m}}$, $BTD_{11-12\mu\text{m}}$, and $BTD_{11-13.3\mu\text{m}}$), the priori state or
420 first guessed vectors (include CTT, cloud emissivity ε at $11\mu\text{m}$, and $\beta[12/11\mu\text{m}]$), the
421 forward radiative transfer model (based on Eq. (2) in the [CLP retrieval algorithm](#)), and
422 the error covariance matrices of the priori state vectors (x_a) and the differences between
423 observations and the forward radiative transfer model of $M(x)$, respectively. As a
424 nonlinear least squares fitting problem, the classical Levenberg-Marquardt iteration
425 method is used here to minimize the cost function of ζ , which can be written as follows
426 (Levenberg, 1944):

$$427 \delta x = (Cov_a^{-1} + K^T Cov_y^{-1} K)^{-1} (K^T (Cov_y^{-1} [y - M(x)]) + Cov_a^{-1} [x_a - x]), \quad (6)$$

428 where K signifies the Jacobi or Kernel matrix. The optimal values of CTT, cloud
429 emissivity, and $\beta[12/11\mu\text{m}]$ will be obtained when the iteration converges the satellite
430 observation vectors of y . It is worth noting that the beta ratio (β) plays a specific role in
431 this retrieval algorithm by analytically solving equations in the Jacobi matrix stated in
432 Eq. (6), thereby resulting in a significant enhancement of operational processing
433 efficiency. After obtaining the optimal CTT, the matched GFS-NWP temperature
434 profile is utilized to interpolate the corresponding cloud top height and pressure. For
435 more detailed information on the CTP retrieval algorithm of H8/9-AHI, please refer to
436 the study from Min et al., 2020.

437 In contrast, the successful retrieval of cloud base properties requires more inputs such
438 as cloud mask, type, top height, and optical and microphysical properties (convert to
439 cloud water path, CWP, unit = g/m^2) as discussed in Sections 3.1, 3.2, and 3.4. Wang
440 et al. (2023) have recently developed and improved a new CBP retrieval algorithm for

删除了: CTP

442 GEO H8/9-AHI, which refers to the CLAVR-x cloud base properties algorithm (Clouds
443 from AVHRR Extended, NOAA's operational cloud processing system for the AVHRR)
444 (Wang et al., 2024; Noh et al., 2017). This algorithm can only be executed during the
445 daytime (solar zenith angle $< 65^\circ$) because it relies on cloud top height (CTH) and cloud
446 water path to calculate the two linear fitting coefficients, namely slope (A_1) and
447 intercept (A_2) (Noh et al., 2017). These two coefficients are determined through
448 piecewise fitting using the CTH, CWP, and cloud base height (CBH) data obtained
449 from the joint CloudSat/CALIPSO (Cloud-Aerosol Lidar and Infrared Pathfinder
450 Satellite Observation) product (Noh et al., 2017). Once the two corresponding fitting
451 coefficients are obtained, the cloud geometric thickness can be calculated as follows:

$$452 \quad CGT = A_1 \times CWP + A_2, \quad (7)$$

453 After that, the CBH can be easily calculated using the formula $CBH = CTH - CGT$.

454 Previous studies have validated the CTH and CBH products obtained through the
455 same algorithms used for the H8 satellite, leveraging joint CloudSat/CALIPSO product
456 (Wang et al., 2024; Wang et al., 2022; Min et al., 2020; Min et al., 2017b). The mean
457 absolute error (MAE) and standard deviation (STD) for GEO satellite CTH are reported
458 as 3.18 km and 3.75 km, respectively, with a noticeable increase associated with higher
459 CTH values. Additionally, the MAE and root-mean-square error (RMSE) for CBH,
460 retrieved by the same GEO CLAVR-x algorithm, stand at 1.938 km and 2.91 km, as
461 reported in prior studies (Wang et al., 2024; Min et al., 2020). In Figure 5, CTH
462 comparisons between the H9/AHI GEO satellite and MODIS are presented for 18:50
463 UTC on October 8, 2023, and 04:30 UTC on July 10, 2023. The figure well
464 demonstrates consistent CTH values and horizontal distributions derived from both
465 H9/AHI and MODIS datasets.

466

467 3.4 Cloud optical and microphysical properties

468 The cloud optical thickness (COT or τ_{cld}) and particle effective radius (CER or r_{cld} ,
469 unit= μm) (or cloud optical and microphysical properties) primarily characterizes the
470 radiative properties of clouds, highlighting their influence on the equilibrium of Earth's
471 radiation budget (Platnick et al., 2017). These two parameters are commonly used in a
472 general circulation model (GCM) to define cloud parameterization schemes for climate
473 modeling (Chou et al., 1998). The cloud optical and microphysical properties algorithm
474 during the daytime (solar zenith angle $< 65^\circ$) utilizes the reflected solar radiation
475 measured by a non-absorbing channel (0.64 μm) to retrieve cloud optical thickness (τ_{cld}).

476 Additionally, it uses the reflected solar radiation measured by an absorbing channel
 477 (2.23 μm) to retrieve cloud particle effective radius (r_{cld}) (Walther et al., 2011). The
 478 fundamental physical principle of this algorithm is to leverage the sensitivities of the
 479 non-absorbing and absorbing channels to cloud optical thickness (τ_{cld}) and cloud
 480 particle effective radius (r_{cld}) in the atmospheric radiative transfer process, as
 481 demonstrated by a previous study (Nakajima and King, 1990).

482 The water and ice cloud optical and radiative properties look-up tables (LUT) with a
 483 modified Gamma size distribution for fast retrieval were built based on spherical
 484 particle with the scattering properties given by the Mie theory and MODIS Collection-
 485 6 severely roughened aggregated columns ice crystal (Min et al., 2017a; Platnick et al.,
 486 2017; Baum et al., 2007), respectively. By utilizing the similar 1DVAR algorithm
 487 discussed in Section 3.3, along with water/ice cloud LUTs, observed reflectance at 0.64
 488 and 2.23 μm channels, and additional ancillary data, the optimal cloud optical thickness
 489 (τ_{cld}) and cloud particle effective radius (r_{cld}) can be iteratively calculated using the OE
 490 algorithm (Walther et al., 2011). Differing from Equation (2), the variables or first-
 491 order partial derivative from forward cloud reflectance model in the Jacobi matrix are
 492 derived from a formula for solar reflectance observed by satellite, which can be written
 493 as follows (Nakajima and King, 1990):

$$494 \quad R_{obs} = R_{cld} + \frac{A_s}{1 - A_s R'_{cld}} T_{cld} T'_{cld}, \quad (8)$$

495 where R_{obs} is the total cloud bidirectional reflectance function at the top of the
 496 atmosphere (TOA). A_s is the albedo at the Lambertian surface of a uniform single-
 497 layer cloud. R_{cld} and T_{cld} signify the cloud reflectance and downward transmittance
 498 (diffuse and direct), respectively. R'_{cld} and T'_{cld} are the cloud spherical albedo and the
 499 transmittance below the cloud, respectively. After retrieving τ_{cld} and r_{cld} , ice and liquid
 500 cloud water paths (IWP/LWP) are calculated using empirical formulas (Bennartz, 2007;
 501 Heymsfield et al., 2007), which are expressed as follows:

$$502 \quad LWP = \frac{5}{9} \tau_{cld} T_{cld} \rho, \quad (9)$$

$$503 \quad IWP = \frac{\tau_{cld}^{1/0.84}}{0.065}, \quad (10)$$

504 where ρ is the density of liquid water (=1.0 g/cm^3).

505 Figure 6 shows the cloud optical depth and effective radius comparisons between the
 506 H9/AHI GEO satellite and MODIS (Platnick et al., 2017) at 05:40 UTC on October 30,
 507 2023. We find consistent retrieval results between these two different COT and CER

删除了: the

509 products. Besides, Figures 6e and 6f respectively show the comparisons of the [one year](#)
 510 COT and CER from MODIS and H9/AHI data over the SCS with the related scores,
 511 such as MAE, MBE, R and RMSE. The differences are likely to be attributed to the
 512 different spatial resolutions and retrieval algorithms used between these two satellite
 513 products (Letu et al., 2019; Wang et al., 2024).

515 3.5 Layered precipitable water and atmospheric instability indices

516 The atmospheric temperature and humidity profiles provide valuable information
 517 about the vertical distribution of water vapor and temperature at various altitudes. This
 518 is very crucial for studying cloud formation, precipitation patterns, and the intricate
 519 processes of the water cycle, and accurate numerical weather forecasting and climate
 520 modeling (Charlesworth et al., 2023; Zheng et al., 2015; Li et al., 2016; Zhu et al.,
 521 2023). In this investigation, the layered precipitable water (LPW) product obtained
 522 from H8/9-AHI only provides clear-sky (refer to the flowchart in Figure 1) temperature
 523 and humidity profiles and atmospheric instability indices. The next few satellite
 524 products [described](#) in Sections 3.6 and 3.7 will also be processed only in clear-sky
 525 pixels. The temperature and humidity profiles will be integrated into three distinct
 526 layers for the output satellite product (High layer: from 700 to 300 hPa; Middle layer:
 527 from 900 to 700 hPa; Low layer: from the surface to 900 hPa).

528 This physics-based LPW retrieval algorithm uses the BT observations at 6.2, 6.9, 7.3,
 529 8.5, 10.4, 11.2, 12.3, and 13.3 μm channels to retrieve temperature and humidity
 530 profiles. Since the temperature and humidity profiles can only be retrieved from clear-
 531 sky pixels, we can express the forward IR radiative transfer equation observed by
 532 satellite sensor as follows (Li et al., 2012; Li et al., 2000):

$$533 \quad I_{obs}(\lambda) = \varepsilon_s(\lambda)B_s(\lambda)T_s(\lambda) - \int_0^{p_s} B(\lambda)dT(\lambda; 0, p) + [1 -$$

$$534 \quad \varepsilon_s(\lambda)] \int_0^{p_s} B(\lambda)dT'(\lambda; 0, p), \quad (11)$$

535 where T is the atmospheric transmittance above the pressure p . Subscript s signifies the
 536 surface, $T' = T_s^2/T$. Similar to the OE method mentioned above, the cost function for
 537 retrieving temperature and humidity profiles can be written as follows:

$$538 \quad \zeta = [x - x_a]^T \gamma Cov_a^{-1} [x - x_a] + [y - M(x)]^T Cov_y^{-1} [y - M(x)], \quad (12)$$

539 where the new added variable γ is the regularization parameter (or smoothing factor)
 540 compared to Eq. (5). The introduction of the parameter γ aims to achieve faster
 541 convergence and improve solution stability. The iterative 1DVAR algorithm can

删除了: four months

删除了:

删除了:

删除了: λ

删除了:

547 increase or decrease parameter γ by determining the first-order variation of Eq. (11) (Li
548 et al., 2000). The first guessed temperature and humidity profiles for iterative retrieval
549 are obtained from spatial-temporally matched GFS-NWP data.

550 After retrieving the optimal temperature and humidity profiles, it will calculate five
551 atmospheric instability indices, including LI (Lifted Index), CAPE (Convective
552 Available Potential Energy), TT (Total Totals), KI (K Index), and SI (Showalter Index).
553 In weather forecasting, these indices can characterize the degree of development of
554 atmospheric instability features and provide the forecaster with a general idea of the
555 convective forcing. For instance, the LI represents the level of atmospheric
556 thermodynamic instability. A positive LI value indicates stability ($0 < LI$), while a
557 negative LI value suggests varying degrees of instability ($-3 < LI < 0$ marginally unstable,
558 $-6 < LI < -3$ moderately unstable, $-9 < LI < -6$ very unstable, and $LI < -9$ extremely unstable)
559 (Fernando et al., 2021). The valid ranges and usages of these five atmospheric
560 instability indices could refer to Table 1 and the study from Li et al., 2012. Note that,
561 considering the specific retrieval efficiency (processing LPW over the SCS region takes
562 approximately 20~25 minutes) of the H8/9-AHI LPW product, we have set the retrieval
563 frequency for LPW to 30 minutes.

564 Figure 7 presents a comparison between the LPW, encompassing total precipitable
565 water and water vapors at low, middle, and high layers, derived from the H9/AHI GEO
566 satellite and ERA5 reanalysis data at 09:00 UTC on January 4, 2023, specifically over
567 the SCS. The right column panel displays associated H9/AHI CAPE, K, LI, and
568 Showalter indices. Except for the water vapors at the high layer (700-300hPa), the
569 remaining LWP products exhibit negligible differences compared to the ERA5
570 reanalysis data in Figure 7.

571 To further validate the LPW products derived from H9/AHI, we conducted
572 comparisons against ERA5 reanalysis data for LPWs over a four-month period
573 mentioned above (January, April, July, and October of 2023). Figure 8 depicts the
574 comparison results for total precipitable water and LPWs at three distinct layers. The
575 correlation coefficients (R) for the LPWs at low, middle, and high layers, along with
576 total precipitable water, are respectively 0.919, 0.784, 0.725, and 0.876. These high
577 correlation coefficients indicate the relatively high quality of this product from the
578 NANO_SCS system.

579

580 *3.6 Land and sea surface temperatures*

删除了: 7

删除了: 849

删除了: 831

删除了: 69

585 Land and sea surface temperatures (LST and SST) are essential variables frequently
 586 utilized in climate research community (Cai et al., 2022; Hong et al., 2022). In this
 587 study, we incorporated a classical land surface temperature algorithm (Ulivieri and
 588 Cannizzaro, 1985) into the NANO_SCS system, using split-windows channels of H8/9-
 589 AHI (11.2 and 12.3 μm). This modified algorithm was also implemented as the
 590 operational LST algorithm for the FY-4A GEO satellite (Dong et al., 2023) in China
 591 Meteorological Administration (CMA), which can be easily expressed as follows:

$$592 \quad LST = C + A_1 BT_{11\mu\text{m}} + A_2 (BT_{11\mu\text{m}} - BT_{12\mu\text{m}}) + A_3 \varepsilon_s + D (BT_{11\mu\text{m}} -$$

$$593 \quad BT_{12\mu\text{m}}) (\sec\theta - 1), \quad (13)$$

594 where C , A_{1-3} , and D are the fitting coefficients, respectively. θ represents the satellite
 595 zenith angle. ε_s is the surface emissivity. To account for the uncertainties in the LST
 596 algorithm caused by water vapor, we conducted regression analysis using MODTRAN
 597 V4.2 (Min et al., 2022; Berk et al., 2000; Dong et al., 2023) to derive fitting coefficients
 598 for four distinct groups: daytime dry, daytime moist, nighttime dry, and nighttime moist
 599 conditions. A threshold of water vapor content = 2.0 g/cm^2 was utilized to classify the
 600 atmosphere as either dry or moist. This threshold value was obtained from matched
 601 GFS-NWP data.

602 The classical and simplified Non-Linear Sea Surface Temperature (NLSST)
 603 algorithm was used here to retrieve SST of H8/9-AHI (Walton et al., 1998), which is
 604 expressed as follows:

$$605 \quad SST = a_0 + a_1 BT_{11\mu\text{m}} + a_2 (BT_{11\mu\text{m}} - BT_{12\mu\text{m}}) + a_3 (BT_{11\mu\text{m}} -$$

$$606 \quad BT_{12\mu\text{m}}) (\sec\theta - 1), \quad (14)$$

607 where a_{0-3} are the fitting coefficients. The NOAA latest OISST (optimum interpolation
 608 sea surface temperature) are used here to obtain fitting coefficients in Eq. (14) (Huang
 609 et al., 2021; Reynolds et al., 2007). This global SST dataset, with a $0.25^\circ \times 0.25^\circ$
 610 horizontal resolution, covers the period from 1981 to the present.

611 Figure 9 shows the LST and SST comparisons between H9/AHI GEO satellite and
 612 MODIS at 18:40 UTC on October 29, 2023. From this figure, we find consistent results
 613 of LST and SST between our results and MODIS official products. Figures 9e and 9f
 614 also shows the comparisons of the [one year](#) LST and SST from MODIS and H9/AHI
 615 data over the SCS. The correlation coefficients (R) of these two products are about 0.96.

616
 617 *3.7 Vegetation and water indices*

删除了: the

删除了: four months

删除了: 7

621 Vegetation and water indices, such as NDVI (Normalized Difference Vegetation
 622 Index), NDSI (Normalized Differential Snow Index), NDWI (Normalized Differential
 623 Water Index), and LSWI (Land Surface Water Index), are commonly utilized for
 624 climate change, vegetation growth, urbanization, flood monitoring, etc. (Zheng et al.,
 625 2021)(Hall et al., 1995)(Xiao et al., 2006)(Gu et al., 2007). In the NANO_SCS system,
 626 these indices are calculated for clear-sky pixels during daytime using H8/9-AHI and
 627 are expressed as follows:

$$628 \quad NDVI = (Ref_{0.86\mu m} - Ref_{0.64\mu m}) / (Ref_{0.86\mu m} + Ref_{0.64\mu m}), \quad (15)$$

$$629 \quad NDSI = (Ref_{0.64\mu m} - Ref_{1.6\mu m}) / (Ref_{0.64\mu m} + Ref_{1.6\mu m}), \quad (16)$$

$$630 \quad NDWI = (Ref_{0.86\mu m} - Ref_{2.23\mu m}) / (Ref_{0.86\mu m} + Ref_{2.23\mu m}), \quad (17)$$

$$631 \quad LSWI = (Ref_{0.86\mu m} - Ref_{1.6\mu m}) / (Ref_{0.86\mu m} + Ref_{1.6\mu m}), \quad (18)$$

632 where *Ref* represents the reflectance observed by satellite visible and near infrared
 633 bands during the daytime. Unfortunately, in this study, the lack of a 0.47 μ m channel
 634 prevents the computation of the Enhanced Vegetation Index (EVI). Figure 10 shows
 635 the clear-sky NDVI, NDSI, NDWI, and LSWI maps from H9/AHI at 04:00 UTC on
 636 December 1, 2023 over the SCS, which were generated by the NANO_SCS system.

637

638 4. Data availability

639 The Japanese Himawari-8 (H8) and Himawari-9 (H9) geostationary (GEO)
 640 satellites are strategically positioned over the South China Sea (SCS), having been
 641 launched on October 7, 2014, and November 2, 2016, respectively. It mainly provides
 642 cloud mask, fraction, height, phase, optical and microphysical properties, layered
 643 precipitable water, and sea surface temperature products, within a temporal resolution
 644 of 10 minutes and a gridded resolution of 0.05° × 0.05°. Users can freely access sample
 645 HDF-formatted files and data download instruction in PDF format of the South China
 646 Sea datasets at <https://doi.org/10.6084/m9.figshare.25015853> (Liu Jian, 2024). Besides,
 647 for accessing related NRT satellite products, a quick-view website URL is provided:
 648 [<http://meteorsatellite.hellosea.org.cn/#/index>]. Data can be download via FTP (File
 649 Transfer Protocol) using the address [FTP://www.hellosea.org.cn:10021](ftp://www.hellosea.org.cn:10021), with the login
 650 credentials being 'smlweix' and the password 'sml#456@'.

651

652 5. Summary

653 This investigation provides a comprehensive introduction to the key GEO satellite
 654 science products generated by the NANO_SCS system and their evaluation. It offers

删除了: 1.6

删除了: 0.

删除了: 64

删除了: 1.6

删除了: 0.64

删除了: 64

删除了: 64

删除了: T

删除了: he Japanese Himawari-8/9 (H8/9) geostationary (GEO) satellites are strategically positioned over the South China Sea (SCS), spanning from November 3, 2022, to the present.

删除了: i

删除了: ng

删除了: to

删除了: , data download FTP (File Transfer Protocol), and user account information (password) are respectively the URLs: [<http://meteorsatellite.hellosea.org.cn/#/index>], <ftp://www.hellosea.org.cn>, and smlweix (sml#456@).

674 near-real-time atmospheric and oceanic science products of Himawari-8/9
675 geostationary satellites over the South China Sea from November 13, 2022, to the
676 present. Positioned at 140.7°E and 0° ~~latitude~~, the H8/9 geostationary satellites mainly
677 cover East Asia, Oceania, and the Indian Ocean. The standard NRT Level-2 satellite
678 science products encompass the region between 0° to 40°N latitude and 100°E to 140°E
679 longitude with a grid resolution of 0.05° × 0.05° and a 10-minute interval (except for
680 LPW products, retrieved every 30 minutes). These products are derived from 14
681 spectral channels with a 4km horizontal resolution.

删除了: longitude

682 The NANO_SCS system provides a range of atmospheric and oceanic products,
683 including cloud mask, fraction, height, phase, optical and microphysical properties,
684 layered precipitable water, land surface temperature, sea surface temperature, and more.
685 These near-real-time satellite products were rigorously evaluated against independent
686 datasets, including MODIS satellite-based products and ERA5 reanalysis data. The
687 results highlight strong consistency between NRT H8/9 geostationary satellite
688 atmospheric and oceanic science products and the reference data from similar sensors
689 and ERA5 over the South China Sea.

690 Future continuation of atmospheric and oceanic science products generated by the
691 NANO_SCS system is also operated and secured by the Southern Marine Science and
692 Engineering Guangdong Laboratory (Zhuhai) in China. Preparations are underway for
693 new products such as atmospheric motion vectors (AMV) and quantitative precipitation
694 estimates (QPE) in near-real-time production. Besides, the qualities of current GEO
695 satellite products will be further validated and enhanced, Chinese FY-4C GEO satellite,
696 scheduled for launch in 2025 or 2026, will offer higher spatial resolution and additional
697 channels, including an IR hyperspectral sounder, to further extend and improve the
698 NANO_SCS-system-based data records for atmospheric and oceanic parameters.

删除了: in the future

699
700

701 **Author contributions.** JL and MM contributed to designing the research; MM, JL, and
702 WW implemented the research and wrote the original draft; JL supervised the research;
703 all co-authors revised the paper and contributed to the writing.

704

705 **Competing interests.** The contact author has declared that none of the authors has any
706 competing interests.

707

710 **Disclaimer.** Publisher’s note: Copernicus Publications remains neutral with regard to
711 jurisdictional claims in published maps and institutional affiliations.

712

713 **Acknowledgments.** The authors would like to thank JMA, U.S. NASA MODIS group
714 and ECMWF for freely providing Himawari-8/9 (<ftp.ptree.jaxa.jp>), MODIS
715 (<https://search.earthdata.nasa.gov/search>), and ERA5 reanalysis
716 (<https://cds.climate.copernicus.eu/cdsapp#!/home>) data. The authors also would like to
717 thank NOAA for freely providing GFS-NWP
718 (<https://nomads.ncep.noaa.gov/pub/data/nccf/com/gfs/>) and OISST
719 ([https://www.ncei.noaa.gov/data/sea-surface-temperature-optimum-
720 interpolation/v2.1/access/avhrr/](https://www.ncei.noaa.gov/data/sea-surface-temperature-optimum-interpolation/v2.1/access/avhrr/)) data, and the GOES-R AWG. Besides, we also thanks
721 Dr. Lixin Dong of China National Satellite Meteorological Center who freely provide
722 LST algorithm code. This study was supported by the Southern Marine Science and
723 Engineering Guangdong Laboratory (Zhuhai) (Grant SML2021SP102 and
724 SML2022SP401), National Natural Science Foundation of China under Grants
725 42175086, FengYun Meteorological Satellite Innovation Foundation under Grant FY-
726 APP-ZX-2022.0207, Innovation Group Project of Southern Marine Science and
727 Engineering Guangdong Laboratory (Zhuhai) (No. SML2023SP208). Finally, we
728 would also like to thank the editor and anonymous reviewers for their thoughtful
729 suggestions and comments.

730

731

732

733

734

735

736

737

738

739

删除了: ←



749 **References**

- 750 Baum, B. A., P. Yang, S. Nasiri, A. J. Heidinger, A. Heymsfield, and J. Li: Bulk
751 scattering properties from the remote sensing of ice clouds. Part III: High
752 resolution spectral models from 100 to 3250 cm⁻¹, *Journal of Applied*
753 *Meteorology and Climatology*, *46*, 423 - 434, doi:10.1175/JAM2473.1, 2007.
- 754 Bennartz, R.: Global assessment of marine boundary layer cloud droplet number
755 concentration from satellite, *Journal of Geophysical Research - Atmospheres*,
756 *112*, D02201, doi:10.1029/2006JD007547, 2007.
- 757 Berk, A., G. P. Anderson, P. K. Acharya, J. H. Chetwynd, L. S. Bernstein, E. P. Shettle,
758 M. W. Matthew, and S. M. Adler-Golden (2000), MODTRAN4 user's manual,
759 edited, Air Force Research Laboratory.
- 760 Bessho, K., et al.: An introduction to Himawari-8/9—Japan's new-generation
761 geostationary meteorological satellites, *Journal of the Meteorological Society*
762 *of Japan*, *94*, 151-183, doi:10.2151/jmsj.2016-009, 2016.
- 763 Cai, W., B. Ng, G. Wang, A. Santoso, L. Wu, and K. Yang: Increased ENSO sea surface
764 temperature variability under four IPCC emission scenarios, *Nature Climate*
765 *Change*, *12*, 228–231, 2022.
- 766 Charlesworth, E., et al.: Stratospheric water vapor affecting atmospheric circulation,
767 *Nature Communications*, *14*, 3925, doi:10.1038/s41467-023-39559-2, 2023.
- 768 Chou, M.-D., M. J. Suarez, C.-H. Ho, M. M.-H. Yan, and K.-T. Lee: Parameterizations
769 for cloud overlapping and shortwave single-scattering properties for use in
770 general circulation and cloud ensemble models, *J Climate*, *11*, 202-214,
771 doi:10.1175/1520-0442(1998)011<0202:PFCOAS>2.0.CO;2, 1998.
- 772 Ding, Y., and Y. Liu: Onset and the evolution of the Summer Monsoon over the South
773 China Sea during SCSMEX Field Experiment in 1998, *Journal of the*
774 *Meteorological Society of Japan*, *179*, 255-276, doi:10.2151/jmsj.79.255, 2001.
- 775 Dong, L., S. Tang, F. Wang, M. Cosh, X. Li, and M. Min: Inversion and validation of
776 FY-4A official land surface temperature product, *Remote Sensing*, *15*, 2437,
777 doi:10.3390/rs15092437 2023.
- 778 Fernando, M., Millangoda, M., and Premalal, S.: Analyze and Comparison of the
779 Atmospheric Instability Using K-Index, Lifted Index Total Totals Index
780 Convective Availability Potential Energy (CAPE) and Convective Inhibition
781 (CIN) in Development of Thunderstorms in Sri Lanka During Second Inter-
782 Monsoon, *Multi-Hazard Early Warning and Disaster Risks, Cham*, 2021//, 603-
783 614,
- 784 Gu, Y., Brown, J. F., Verdin, J. P., and Wardlow, B. D.: A five-year analysis of MODIS
785 NDVI and NDWI for grassland drought assessment over the central Great Plains
786 of the United States, *Geophysical Research Letters*, *34*, 2007.
- 787 Hall, D. K., Riggs, G. A., and Salomonson, V. V.: Development of methods for mapping
788 global snow cover using moderate resolution imaging spectroradiometer data,
789 *Remote Sensing of Environment*, *54*, 127-140, 1995.
- 790 Heidinger, A., and M. Pavlonis: Gazing at cirrus clouds for 25 years through a split
791 window, part 1: Methodology, *Journal of Applied Meteorology and Climatology*,
792 *48*, 1110-1116, doi:10.1175/2008JAMC1882.1, 2009.
- 793 Heidinger, A. K., A. T. Evan, M. J. Foster, and A. Walther: A naive Bayesian cloud-

794 detection scheme derived from CALIPSO and applied within PATMOS-x,
795 Journal of Applied Meteorology and Climatology, *51*, 1129–1144,
796 doi:10.1175/JAMC-D-11-02.1, 2012.

797 Hersbach, H., et al.: The ERA5 global reanalysis, Quarterly Journal of the Royal
798 Meteorological Society, *146*, 1999–2049, doi:10.1002/qj.3803, 2020.

799 Heymsfield, A. J., S. Matrosov, and B. Baum: Ice water path-optical depth relationships
800 for cirrus and deep stratiform ice cloud layers, J Appl Meteorol, *42*, 1369–1390,
801 doi:10.1175/1520-0450(2003)042<1369:IWPDRF>2.0.CO;2, 2007.

802 Hong, F., W. Zhan, F.-M. Göttsche, Z. Liu, P. Dong, H. Fu, F. Huang, and X. Zhang: A
803 global dataset of spatiotemporally seamless daily mean land surface
804 temperatures: generation, validation, and analysis, Earth System Science Data,
805 *14*, 3091–3113, doi:10.5194/essd-14-3091-2022, 2022.

806 Huang, B., C. Liu, V. Banzon, E. Freeman, G. Graham, B. Hankins, T. Smith, and H.-
807 M. Zhang: Improvements of the Daily Optimum Interpolation Sea Surface
808 Temperature (DOISST) Version 2.1, J Climate, *34*, 2923-2939,
809 doi:10.1175/JCLI-D-20-0166.1, 2021.

810 Husi, L., T. M. Nagao, T. Y. Nakajima, J. Riedi, H. Ishimoto, A. J. Baran, H. Shang, M.
811 Sekiguchi, and M. Kikuchi: Ice cloud properties from Himawari-8/AHI next-
812 generation geostationary satellite: Capability of the AHI to monitor the DC
813 cloud generation process, IEEE Transactions on Geoscience and Remote
814 Sensing, *57*, 3229-3239, doi:10.1109/TGRS.2018.2882803 2019.

815 Jiang, J., T. Zhou, Y. Qian, C. Li, F. Song, H. Li, X. Chen, W. Zhang, and Z. Chen:
816 Precipitation regime changes in High Mountain Asia driven by cleaner air,
817 Nature, doi:10.1038/s41586-023-06619-y, 2023.

818 Kim, D., M. Gu, T.-H. Oh, E.-K. Kim, and H.-J. Yang: Introduction of the advanced
819 meteorological imager of Geo-Kompsat-2a: In-orbit tests and performance
820 validation, Remote Sensing, *13*, 1303, doi:10.3390/rs13071303, 2021.

821 King, M. D., S. C. Tsay, S. E. Planick, M. Wang, and K. N. Liou: Cloud retrieval
822 algorithms: Optical thickness, effective particle radius, and thermodynamic
823 phase, NASA MODIS Algorithm Theoretical Basis Documents, 1997.

824 Koseki, S., K. Tieh-Yong, and T. Chee-Kiat: Effects of the cold tongue in the South
825 China Sea on the monsoon, diurnal cycle and rainfall in the Maritime Continent,
826 Quarterly Journal of the Royal Meteorological Society, *139*, 1566-1582,
827 doi:10.1002/qj.2052, 2013.

828 Lai, R., S. Teng, B. Yi, H. Letu, M. Min, S. Tang, and C. Liu: Comparison of cloud
829 properties from Himawari-8 and FengYun-4A geostationary satellite
830 radiometers with MODIS cloud retrievals, Remote Sensing, *11*, 1703,
831 doi:10.3390/rs11141703, 2019.

832 Letu, H., T. M. Nagao, T. Y. Nakajima, J. Riedi, H. Ishimoto, A. J. Baran, H. Shang, M.
833 Sekiguchi, and M. Kikuchi: Ice cloud properties from Himawari-8/AHI next-
834 generation geostationary satellite: Capability of the AHI to monitor the DC
835 cloud generation process, IEEE Transactions on Geoscience and Remote
836 Sensing, *57*, 3229-3239, doi:10.1109/tgrs.2018.2882803, 2019.

837 Letu, H., et al.: High-resolution retrieval of cloud microphysical properties and surface
838 solar radiation using Himawari-8/AHI next-generation geostationary satellite,
839 Remote Sensing of Environment, 239, 111583, doi:10.1016/j.rse.2019.111583,
840 2020.

841 Levenberg, K.: A method for the solution of certain non-linear problems in least squares,
842 Quarterly of Applied Mathematics, 2, 164-168, 1944.

843 Li, J., W. P. Menzel, T. J. Schmit, and J. Schmetz: Applications of geostationary
844 hyperspectral infrared sounder observations – progress, challenges, and future
845 perspectives, Bulletin of the American Meteorological Society,
846 doi:10.1175/BAMS-D-21-0328.1, 2022a.

847 Li, J., T. J. Schmit, X. Jin, and G. Martin: GOES-R Advanced Baseline Imager (ABI)
848 Algorithm Theoretical Basis Document For Legacy Atmospheric Moisture
849 Profile, Legacy Atmospheric Temperature Profile, Total Precipitable Water, and
850 Derived Atmospheric Stability Indices NOAA Goes-R ATBD, 109, 2012.

851 Li, J., P. Wang, H. Han, J. Li, and J. Zheng: On the assimilation of satellite sounder data
852 in cloudy skies in numerical weather prediction models, Journal of
853 Meteorological Research, 30, 169–182, 2016.

854 Li, J., W. W. Wolf, W. P. Menzel, W. Zhang, H.-L. Huang, and T. H. Achtor: Global
855 soundings of the atmosphere from ATOVS measurements: The algorithm and
856 validation, Journal of Applied Meteorology, 39, 1248–1268, doi:10.1175/1520-
857 0450(2000)039<1248:GSOTAF>2.0.CO;2, 2000.

858 Li, Y., G. Ren, Q. Wang, L. Mu, and Q. Niu: Marine heatwaves in the South China Sea:
859 Tempo-spatial pattern and its association with large-scale circulation, Remote
860 Sensing, 14, 5829, doi:10.3390/rs14225829, 2022b.

861 Liang, Y., M. Min, Y. Yu, X. Wang, and P. Xia: Assessing diurnal cycle of cloud covers
862 of Fengyun-4A geostationary satellite based on the manual observation data in
863 China, IEEE Transactions on Geoscience and Remote Sensing, 61,
864 doi:10.1109/TGRS.2023.3256365, 2023.

865 Liu, B., Y. Liu, G. Wu, J. Yan, J. He, and S. Ren: Asian summer monsoon onset barrier
866 and its formation mechanism, Climate Dynamics, 45, 711–726,
867 doi:10.1007/s00382-014-2296-0, 2014.

868 Liu Jian, Y. J., Lin Chuyong, He Min, Liu Haiyan, Min Min, Wang Wei (2024), Near
869 real-time atmospheric and oceanic science products of Himawari-8/9
870 geostationary satellites over the South China Sea, edited, figshare. Dataset.,
871 doi:<https://doi.org/10.6084/m9.figshare.25015853>.

872 Ma, Z., J. Li, W. Han, Z. Li, Q. Zeng, W. P. Menzel, T. J. Schmit, D. Di, and C.-Y. Liu:
873 Four - dimensional wind fields from geostationary hyperspectral infrared
874 sounder radiance measurements with high temporal resolution, Geophys Res
875 Lett, 48, e2021GL093794, doi:10.1029/2021GL093794, 2021.

876 Martin, D. W., and M. R. Howland: Rainfall over the Arabian Sea during the onset of
877 the 1979 monsoon, Nature, 300, 628–630, 1982.

878 Min, M., et al.: Estimating summertime precipitation from Himawari-8 and global
879 forecast system based on machine learning, IEEE Transactions on Geoscience

880 and Remote Sensing, *57*, 2557-2570, doi:10.1109/TGRS.2018.2874950, 2019.

881 Min, M., B. Chen, N. Xu, X. He, X. Wei, and M. Wang: Nonnegligible diurnal and
882 long-term variation characteristics of the calibration biases in Fengyun-
883 4A/AGRI infrared channels based on the oceanic drifter data, *IEEE*
884 *Transactions on Geoscience and Remote Sensing*, *60*, 1-15,
885 doi:10.1109/TGRS.2022.3160450, 2022.

886 Min, M., J. Deng, C. Liu, N. Lu, X. Hu, L. Chen, J. Guo, P. Zhang, Q. Lu, and L. Wang:
887 An investigation of the implications of lunar illumination spectral changes for
888 Day/Night Band based cloud property retrieval due to lunar phase transition,
889 *Journal of Geophysical Research: Atmospheres*, *122*, 9233-9244,
890 doi:10.1002/2017JD027117, 2017a.

891 Min, M., J. Li, F. Wang, Z. Liu, and W. P. Menzel: Retrieval of cloud top properties
892 from advanced geostationary satellite imager measurements based on machine
893 learning algorithms, *Remote Sensing of Environment*, *239*, 111616,
894 doi:10.1016/j.rse.2019.111616 2020.

895 Min, M., et al.: Developing the science product algorithm testbed for Chinese next-
896 generation geostationary meteorological satellites: Fengyun-4 series, *Journal of*
897 *Meteorological Research*, *31*, 708-719, doi:10.1007/s13351-017-6161-z, 2017b.

898 Mülmenstädt, J., M. Salzmann, J. E. Kay, M. D. Zelinka, P.-L. Ma, C. Nam, J.
899 Kretzschmar, S. Hörnig, and J. Quaas: An underestimated negative cloud
900 feedback from cloud lifetime changes, *Nature Climate Change*, *11*, 508-513,
901 doi:10.1038/s41558-021-01038-1, 2021.

902 Nakajima, T., and M. D. King: Determination of the optical thickness and effective
903 particle radius of clouds from reflected solar radiation measurements. Part I:
904 Theory, *J Atmos Sci*, *48*, 728-750, 1990.

905 Niu, Q., and Y. Feng: Relationships between the typhoon-induced wind and waves in
906 the northern South China Sea, *Geophys Res Lett*, *48*, e2020GL091665,
907 doi:10.1029/2020GL091665, 2021.

908 Noh, Y.-J., J. M. Forsythe, S. D. Miller, C. J. Seaman, Y. Li, A. K. Heidinger, D. T.
909 Lindsey, M. A. Rogers, and P. T. Partain: Cloud-base height estimation from
910 VIIRS. Part II: A statistical algorithm based on A-Train satellite data, *Journal of*
911 *Atmospheric and Oceanic Technology*, *34*, 585-598, doi:10.1175/JTECH-D-
912 16-0110.1, 2017.

913 Parol, F., J. C. Buriez, G. Brogniez, and Y. Fouquart: Information content of AVHRR
914 channels 4 and 5 with respect to the effective radius of cirrus cloud particles, *J*
915 *Appl Meteorol*, *30*, 973-984, 1991.

916 Pavolonis, M.: GOES-R Advanced Baseline Imager (ABI) Algorithm Theoretical Basis
917 Document For Cloud Type and Cloud Phase Version 2.0, NOAA GOES-R
918 ATBD, 1-96, 2010a.

919 Pavolonis, M. J.: Advances in extracting cloud composition information from
920 spaceborne infrared radiances-A robust alternative to brightness temperatures.
921 Part I: Theory, *Journal of Applied Meteorological Climatology*, *49*, 1992-2012,
922 2010b.

923 Pavolonis, M. J., A. K. Heidinger, and T. Uttal: Daytime global cloud typing from
 924 AVHRR and VIIRS: Algorithm description, validation, and comparisons *J Appl*
 925 *Meteorol*, *44*, 804-826, 2005.

926 Platnick, S., M. D. King, S. A. Ackerman, W. P. Menzel, B. A. Baum, J. C. Riédi, and
 927 R. A. Frey: The MODIS cloud products: Algorithms and examples from Terra,
 928 *IEEE Transactions on Geoscience and Remote Sensing*, *41*, 459-473,
 929 doi:10.1109/TGRS.2002.808301, 2003.

930 Platnick, S., et al.: The MODIS cloud optical and microphysical products: Collection 6
 931 updates and examples from Terra and Aqua, *IEEE Transactions On Geoscience*
 932 *and Remote Sensing*, *55*, 502-525, doi:10.1109/TGRS.2016.2610522, 2017.

933 Reynolds, R., T. M. Smith, C. Liu, D. Chelton, K. Casey, and M. Schlax: Daily high-
 934 resolution-blended analyses for sea surface temperature, *J Climate*, *20*, 5473-
 935 5496, doi:10.1175/2007JCLI1824.1, 2007.

936 Rodgers, C. D.: *Inverse methods for atmospheric sounding: Theory and practice*, 2000.

937 Schmit, T. J., P. Griffith, M. M. Gunshor, J. M. Daniels, S. J. Goodman, and W. J. Lebar:
 938 A closer look at the ABI on the GOES-R Series *Bulletin of the American*
 939 *Meteorological Society*, *98*, 681-698 doi:10.1175/BAMS-D-15-00230.1, 2017.

940 Soldi, G., et al.: Space-based global maritime surveillance. Part I: Satellite technologies,
 941 *IEEE Aerospace and Electronic Systems Magazine* *36*, 8-28,
 942 doi:10.1109/MAES.2021.3070862, 2021.

943 Ulivieri, C., and G. Cannizzaro: Land surface temperature retrievals from satellite
 944 measurements, *Acta Astronaut*, *12*, 985-997, doi:10.1016/0094-
 945 5765(85)90026-8, 1985.

946 Viúdez-Mora, A., C.-S. M., J. Calbó, and J. A. González: Modeling atmospheric
 947 longwave radiation at the surface during overcast skies: The role of cloud base
 948 height, *Journal of Geophysical Research: Atmospheres*, *120*, 199-214,
 949 doi:10.1002/2014JD022310, 2015.

950 Walther, A., W. Straka, and A. K. Heidinger: GOES-R Advanced Baseline Imager (ABI)
 951 algorithm theoretical basis document for daytime cloud optical and
 952 microphysical properties (DCOMP), NOAA Goes-R ATBD, 2011.

953 Walton, C. C., W. G. Pichel, J. F. Sapper, and D. A. May: The development and
 954 operational application of nonlinear algorithms for the measurement of sea
 955 surface temperatures with the NOAA polar-orbiting environmental satellites,
 956 *Journal of Geophysical Research*, *103*, 27999-28012, doi:10.1029/98JC02370,
 957 1998.

958 Wang, B., F. Huang, Z. Wu, J. Yang, X. Fu, and K. Kikuchi: Multi-scale climate
 959 variability of the South China Sea monsoon: A review, *Dynamics of*
 960 *Atmospheres and Oceans*, *47*, 15-37, doi:10.1016/j.dynatmoce.2008.09.004,
 961 2009.

962 Wang, F., M. Min, N. Xu, C. Liu, Z. Wang, and L. Zhu: Effects of linear calibration
 963 errors at low temperature end of thermal infrared band: Lesson from failures in
 964 cloud top property retrieval of FengYun-4A geostationary satellite, *IEEE*
 965 *Transactions on Geoscience and Remote Sensing*, *60*, 5001511,

966 doi:10.1109/TGRS.2022.3140348, 2022.

967 Wang, G., S.-P. Xie, T. Qu, and R. X. Huang: Deep South China Sea circulation,
 968 *Geophys Res Lett*, *38*, L05601, doi:10.1029/2010GL046626, 2011.

969 Wang, M., M. Min, J. Li, B. Chen, H. Lin, Z. Yao, N. Xu, and M. Zhang: Applicability
 970 of physics-based and machine-learning-based algorithms of geostationary
 971 satellite in retrieving the diurnal cycle of cloud base height, *Atmospheric
 972 Chemistry and Physics Discussion*, 2024.

973 Wang, X., Q.-Y. Liu, D. Sui, and D. Wang: The imprint of the ENSO activities on the
 974 South China Sea wave climate, *Ocean Dynamics*, *70*, 1315–1323,
 975 doi:10.1007/s10236-020-01400-5, 2020.

976 Wang, X., M. Min, F. Wang, J. Guo, B. Li, and S. Tang: Intercomparisons of cloud mask
 977 product among Fengyun-4A, Himawari-8 and MODIS, *IEEE Transactions on
 978 Geoscience and Remote Sensing*, *57*, 8827–8839,
 979 doi:10.1109/TGRS.2019.2923247 2019.

980 Whitaker, J. S., T. M. Hamill, X. Wei, Y. Song, and Z. Toth: Ensemble data assimilation
 981 with the NCEP global forecast system, *Monthly Weather Review*, *136*, 463–482,
 982 doi:10.1175/2007MWR2018.1, 2008.

983 Xia, P., M. Min, Y. Yu, Y. Wang, and L. Zhang: Developing a near real-time cloud cover
 984 retrieval algorithm using geostationary satellite observations for photovoltaic
 985 plants, *Remote Sensing*, *15*, 1141, doi:10.3390/rs15041141, 2023.

986 Xia, P., L. Zhang, M. Min, J. Li, Y. Wang, Y. Yu, and S. Jia: Accurate nowcasting on
 987 cloud cover at solar photovoltaic plants using geostationary satellite images,
 988 *Nature Communications*, *15*, 1–10, doi:10.1038/s41467-023-44666-1, 2024.

989 **Xiao, X., Boles, S., Frolking, S., Li, C., Babu, J. Y., Salas, W., and Moore, B.: Mapping
 990 paddy rice agriculture in South and Southeast Asia using multi-temporal
 991 MODIS images, *Remote Sensing of Environment*, *100*, 95–113,
 992 <https://doi.org/10.1016/j.rse.2005.10.004>, 2006.**

993 Xu, W., S. A. Rutledge, and K. Chudler: Diurnal cycle of coastal convection in the
 994 South China Sea region and modulation by the BSISO34, 4297–4314,
 995 doi:10.1175/JCLI-D-20-0308.1, 2021.

996 Yang, J., Z. Zhang, C. Wei, F. Lu, and Q. Guo: Introducing the new generation of
 997 Chinese geostationary weather satellites, FengYun-4, *Bulletin of the American
 998 Meteorological Society*, *98*, 1637–1658, doi:10.1175/BAMS-D-16-0065.1,
 999 2017.

1000 Zhao, G., and L. D. Girolamo: Cloud fraction errors for trade wind cumuli from EOS-
 1001 Terra instruments, *Geophys Res Lett*, *33*, L20802, doi:10.1029/2006GL027088,
 1002 2006.

1003 Zheng, J., J. Li, T. J. Schmit, J. Li, and Z. Liu: The impact of AIRS atmospheric
 1004 temperature and moisture profiles on hurricane forecasts: Ike (2008) and Irene
 1005 (2011), *Advances in Atmospheric Sciences*, *32*, 319–335, 2015.

1006 Zheng, Y., L. Tang, and H. Wang: An improved approach for monitoring urban built-up
 1007 areas by combining NPP-VIIRS nighttime light, NDVI, NDWI, and NDBI,
 1008 *Journal of Cleaner Production*, *328*, 129488, doi:10.1016/j.jclepro.2021.129488,

1009 2021.
1010 Zhou, R., X. Pan, Z. Xiaohu, X. Na, and M. Min: Research progress and prospects of
1011 atmospheric motion vector based on meteorological satellite images, *Reviews of*
1012 *Geophysics and Planetary Physics (In Chinese)*, 55, 184-194,
1013 doi:10.19975/j.dqyxx.2022-077, 2024.
1014 Zhu, L., R. Zhou, D. Di, W. Bai, and Z. Liu: Retrieval of atmospheric water vapor
1015 content in the environment from AHI/H8 using both physical and random forest
1016 methods—A case study for typhoon Maria (201808), *Remote Sensing*, 15, 498,
1017 doi:10.3390/rs15020498, 2023.
1018
1019
1020
1021
1022
1023
1024
1025
1026
1027
1028
1029
1030
1031
1032
1033
1034
1035
1036
1037

1038

1039 **Tables and Figures**

1040 **Table 1.** Primary NRT H8/9 GEO satellite atmospheric and oceanic science products
 1041 and related variables generated by the NANO_SCS system.

Product Name (Abbr.)	Variable Name	Valid Value	Unit	Note
Cloud Mask (CLM)	Cloud_Mask	0=Cloudy; 1=Probably cloudy; 2=Probably clear ; 3=Clear	None	
Cloud Fraction (CLF)	Cloud_Fraction	0-100	%	down-sampled 5x5 pixel box
Cloud Type and Phase (CLP)	Cloud_Type	0=Clear; 1=Spare; 2=Liquid water; 3=Supercooled water; 4=Mixed; 5=Optically thick ice; 6=Optically thin ice; 7=Multilayered ice; 8=Uncertainty	None	
	Cloud_Phase	0=Clear; 1=Liquid water; 2=Supercooled water; 3=Mixed; 4=Ice; 5=Uncertainty	None	
Cloud Top Properties (CTP)	Cloud_Top_Height	0-30000	m	
	Cloud_Top_Pressure	0-2000	hPa	
	Cloud_Top_Temperature	0-400	K	
	Cloud_Emissivity_at_11um	0-100	%	
Cloud Optical and Microphysical Properties (COT)	Cloud_Optical_Depth	0-150	None	only daytime
	Cloud_Effective_Radius	0-100	um	only daytime
	Cloud_Liquid_Water_Path	0-1000	g/m ²	only daytime
	Cloud_Ice_Water_Path	0-1000	g/m ²	only daytime
Cloud Base Properties (CBP)	Cloud_Base_Height	0-30000	m	only daytime
	Cloud_Base_Pressure	0-2000	hPa	only daytime
Sea Surface Temperature (SST)	Sea_Surface_Temperature	0-400	K	
Land Surface Temperature (LST)	Land_Surface_Temperature	0-400	K	
Vegetation/Water Indices (NDI)	NDVI (Normalized Difference Vegetation Index)	0-1.0	None	only daytime
	NDSI (Normalized Differential Snow Index)	0-1.0	None	only daytime
	NDWI (Normalized Differential Water Index)	0-1.0	None	only daytime
	LSWI (Land Surface Water Index)	0-1.0	None	only daytime
Layered Precipitable Water (LPW)	Total_Precipitable_Water	0-1000	mm	
	Water_Vapor_High	0-1000	mm	700-300hPa
	Water_Vapor_Middle	0-1000	mm	900-700hPa
	Water_Vapor_Low	0-1000	mm	Surface-900hPa
	CAPE_Index (Convective Available Potential Energy)	0-10000	J/kg	
	K_Index	-100-100	K	
	LI_Index (Lifted)	0-400	K	Stored in Celsius
	Showalter_Index	0-400	K	Stored in Celsius
TT_Index (Total totals)	0-400	K	Stored in Celsius	

删除了: ←



删除了: -100-100

删除了: °C

删除了: -100-100

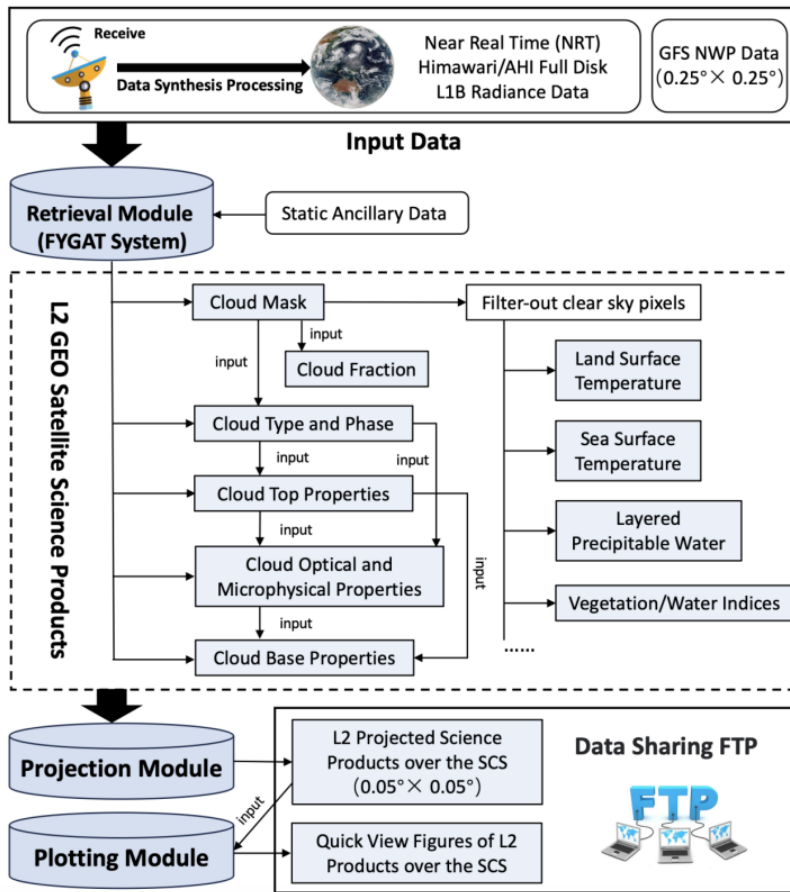
删除了: °C

删除了: -100-100

删除了: °C

1042

1059
1060
1061



1062

1063 **Figure 1.** Flowchart of the NANO_SCS system. Dark gray shading represents key
1064 processing module; light gray shading represents satellite science product.

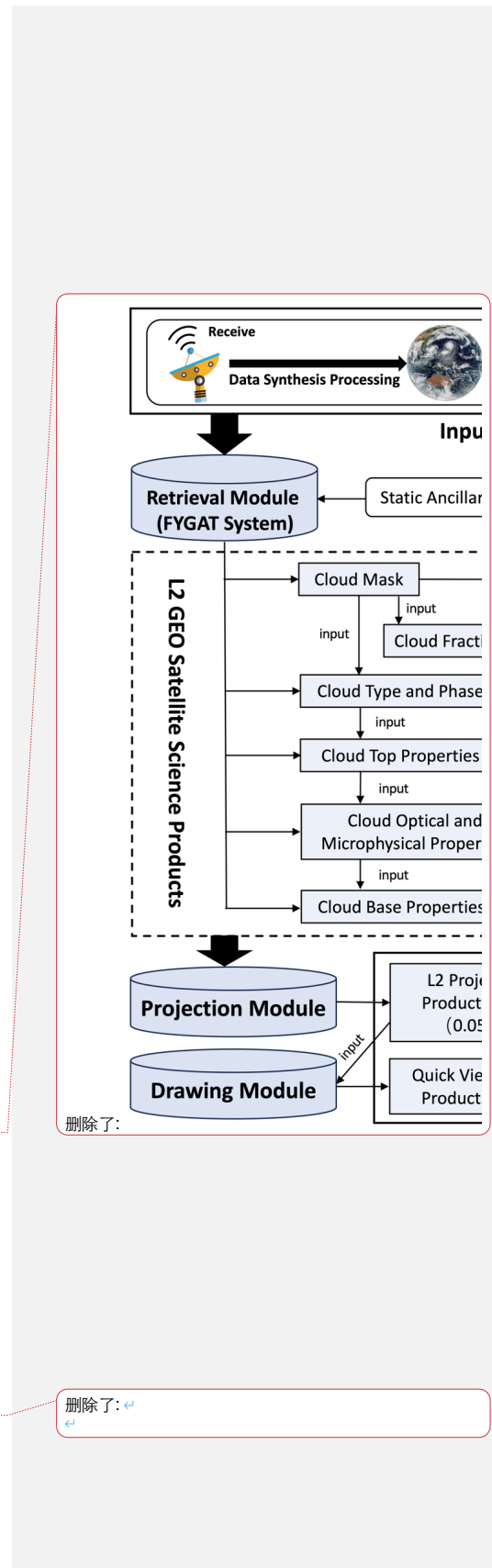
1065

1066

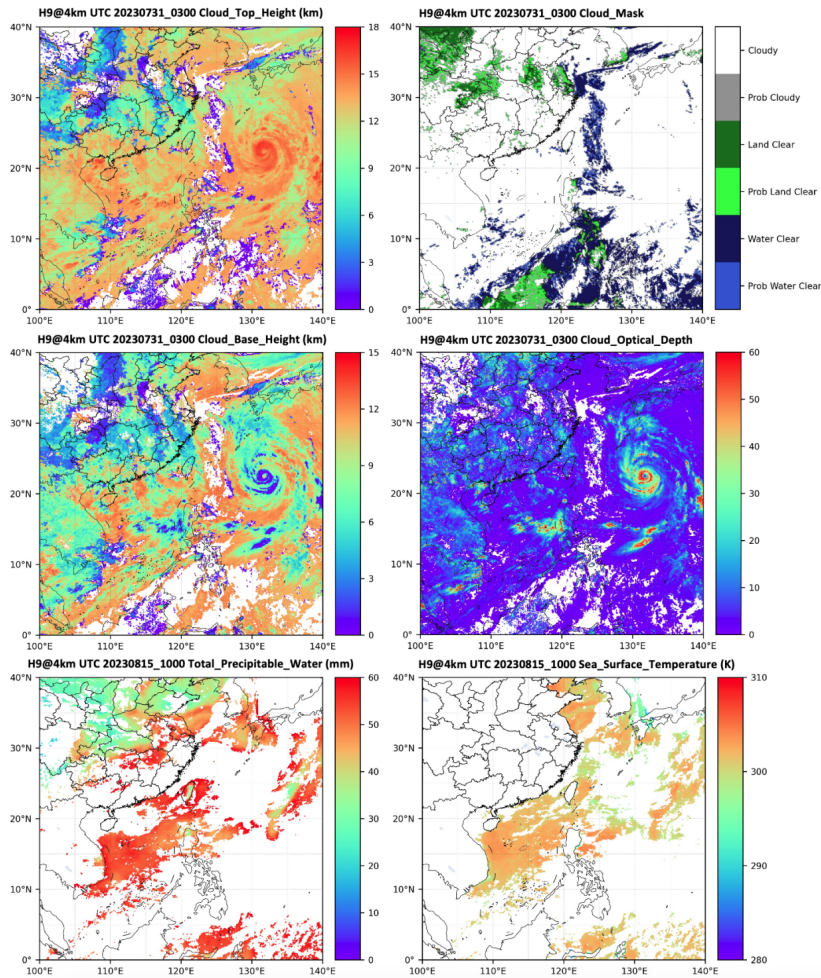
1067

1068

1069



1073
1074



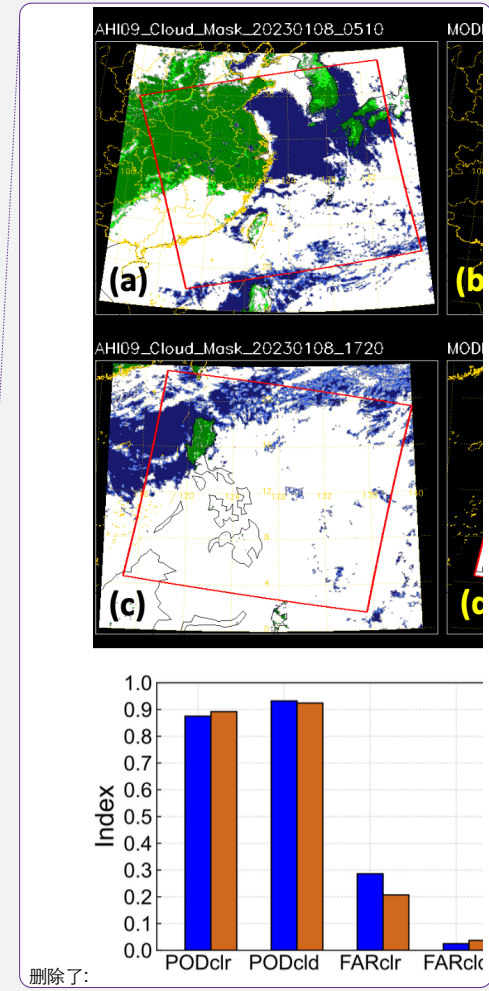
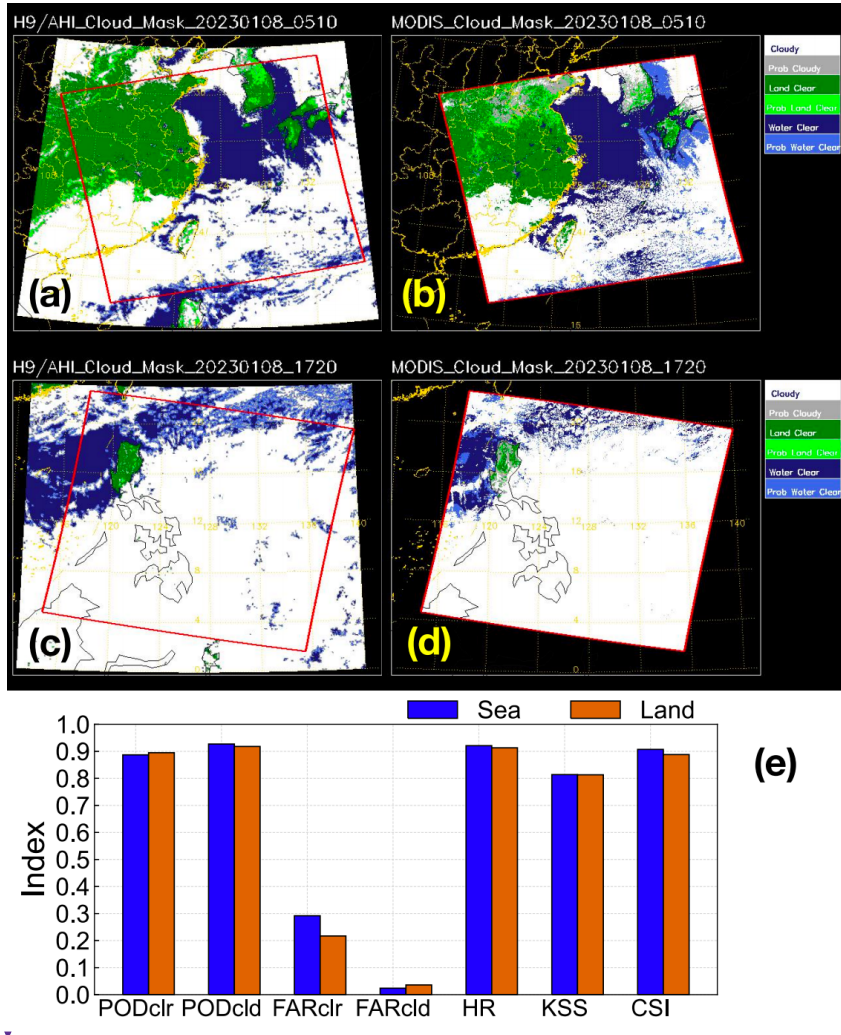
1075
1076 **Figure 2.** H9/AHI GEO satellite cloud top height (left top panel), cloud mask (right top
1077 panel), cloud base height (left middle panel), cloud optical depth (right middle panel)
1078 at 03:00 UTC on July 31, 2023, and atmospheric total precipitable water (left bottom
1079 panel) and sea surface temperature (right bottom panel) at 10:00 UTC on August 15,
1080 2023 over the NANO SCS system.

1081
1082
1083

删除了: SCS

删除了: ←

←



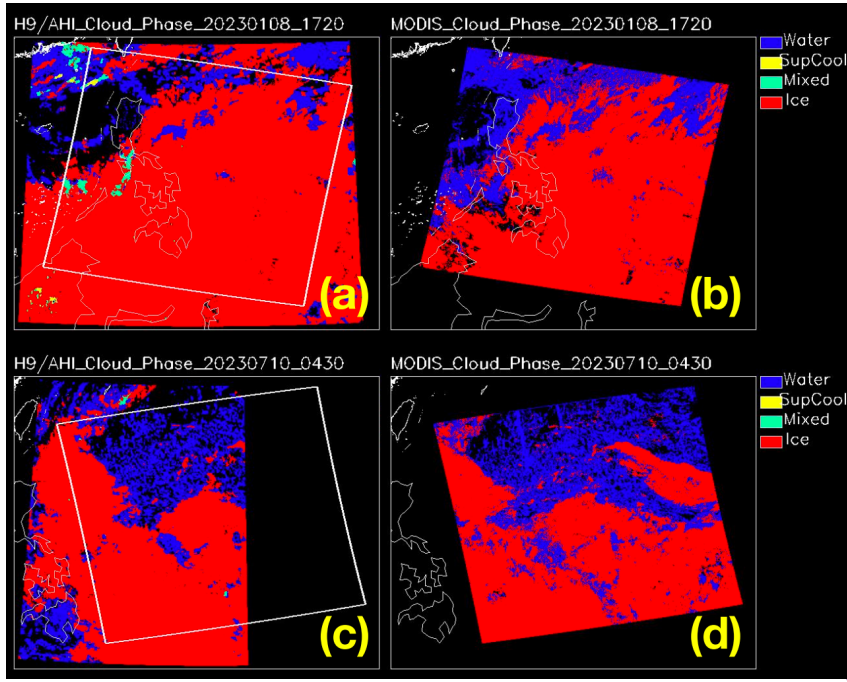
删除了:

删除了: ←

1088
1089
1090
1091
1092
1093
1094
1095
1096
1097

Figure 3. Cloud mask comparisons between (a, c) H9/AHI GEO satellite and (b, d) MODIS at 05:10 (top panel) and 17:20 (middle panel) UTC on January 8, 2023. (e) POD, FAR, HR, and KSS scores of H9/AHI results for all the matched pixels over land (earthy yellow) and sea (blue) in January, April, July, and October of 2023. "clr" and "cld" respectively signify the clear-sky and cloudy-sky pixels.

1100



1101

1102 **Figure 4.** Cloud phase comparisons between (a, c) H9/AHI GEO satellite and (b, d)
 1103 MODIS at 05:10 UTC (top panel) on January 8, 2023 and 04:30 UTC (bottom panel)
 1104 on July 10, 2023.

1105

1106

1107

1108

1109

1110

1111

1112

1113

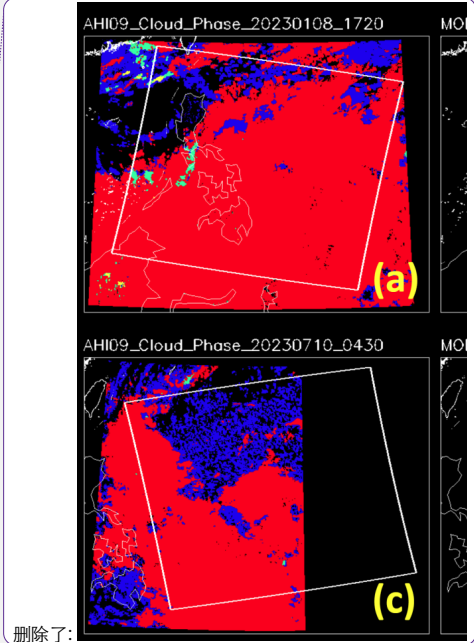
1114

1115

1116

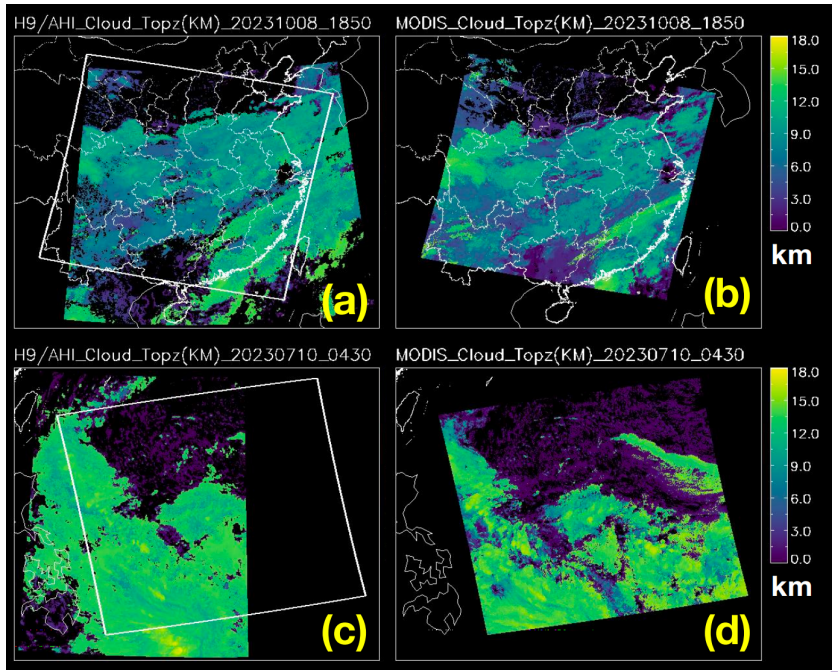
1117

删除了: ←



删除了:

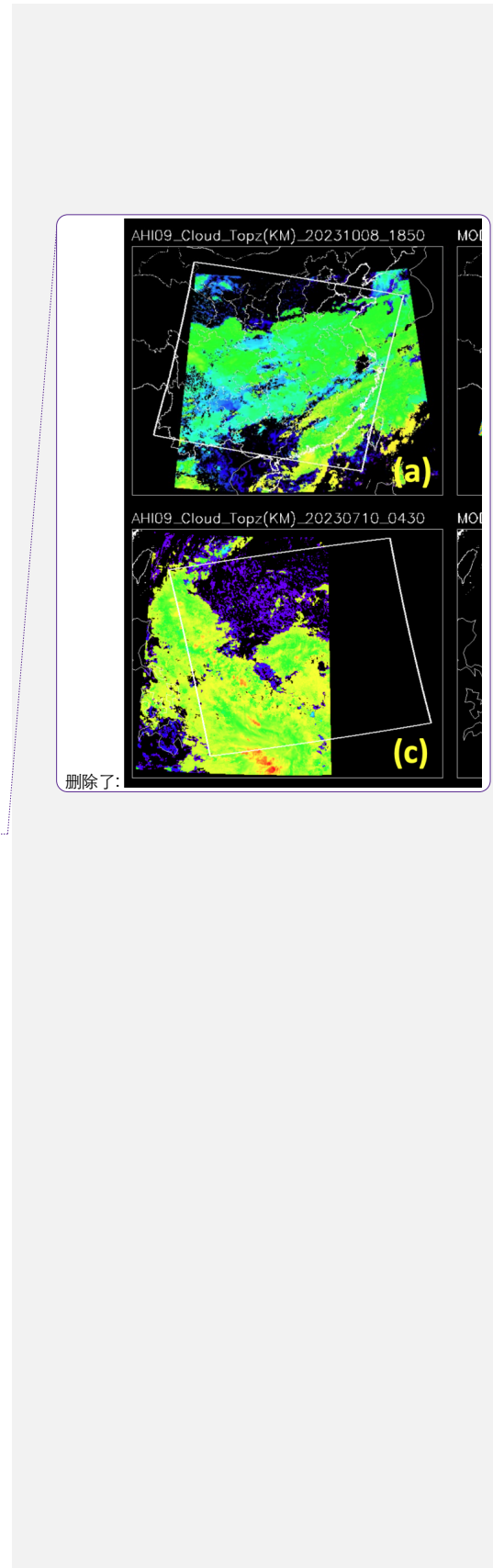
1121
1122



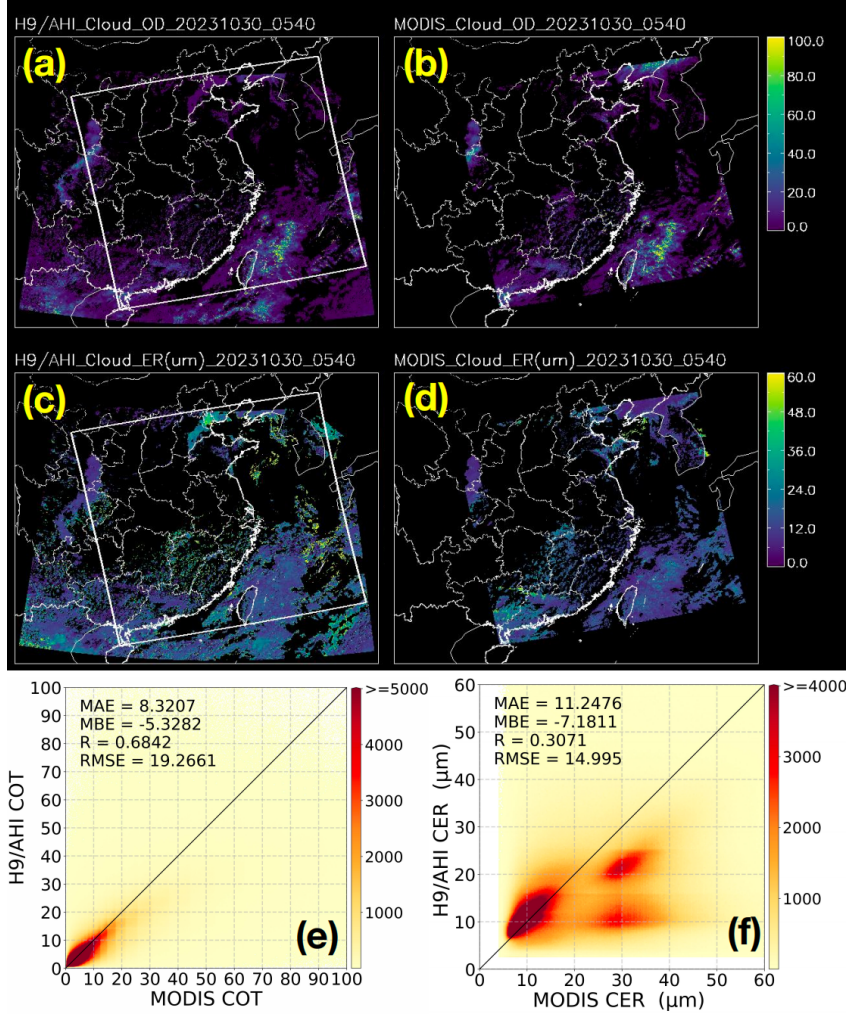
1123

1124 **Figure 5.** Cloud top height comparisons between (a, c) H9/AHI GEO satellite and (b,
1125 d) MODIS at 18:50 UTC (top panel) on October 8, 2023 and 04:30 UTC (bottom panel)
1126 on July 10, 2023.

1127
1128
1129
1130
1131
1132
1133
1134
1135
1136
1137
1138



1140
1141

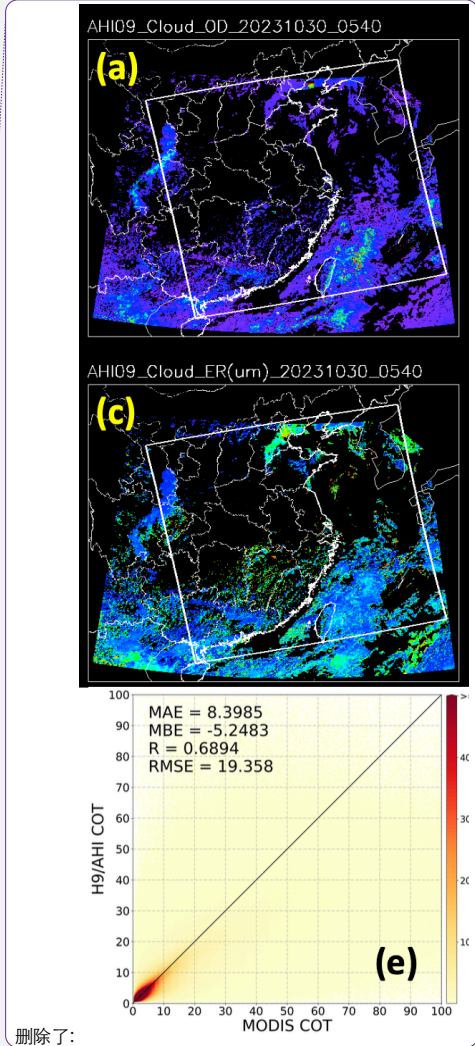


1142

1143 **Figure 6.** Cloud optical depth (top panel) and effective radius (middle panel)
1144 comparisons between (a, c) H9/AHI GEO satellite and (b, d) MODIS at 05:40 UTC on
1145 October 30, 2023. Comparisons of the one year (2023) (e) cloud optical depth and (f)
1146 effective radius from MODIS and H9/AHI data over the NANO_SCS system. The color
1147 bar represents the total number in every bin at an interval of 0.2 of COT or 0.2 μm of
1148 CER.

1149

删除了: ←



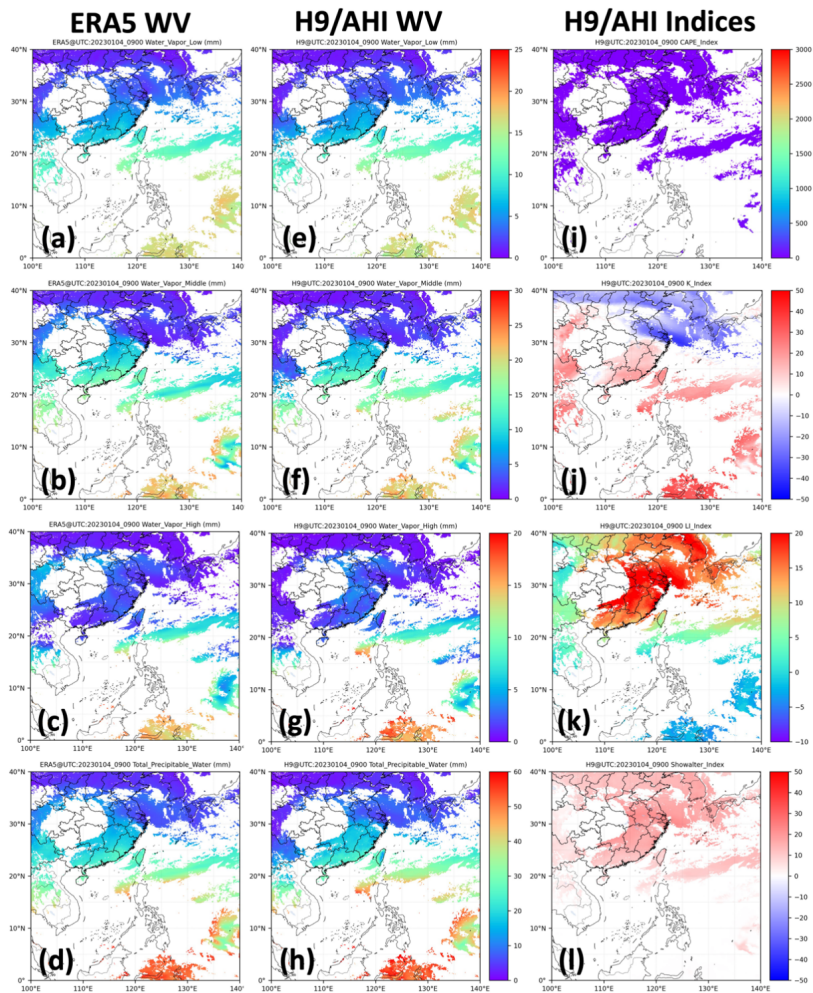
删除了:

删除了: four months

删除了: January, April, July, and October of

删除了: SCS

1156



1157

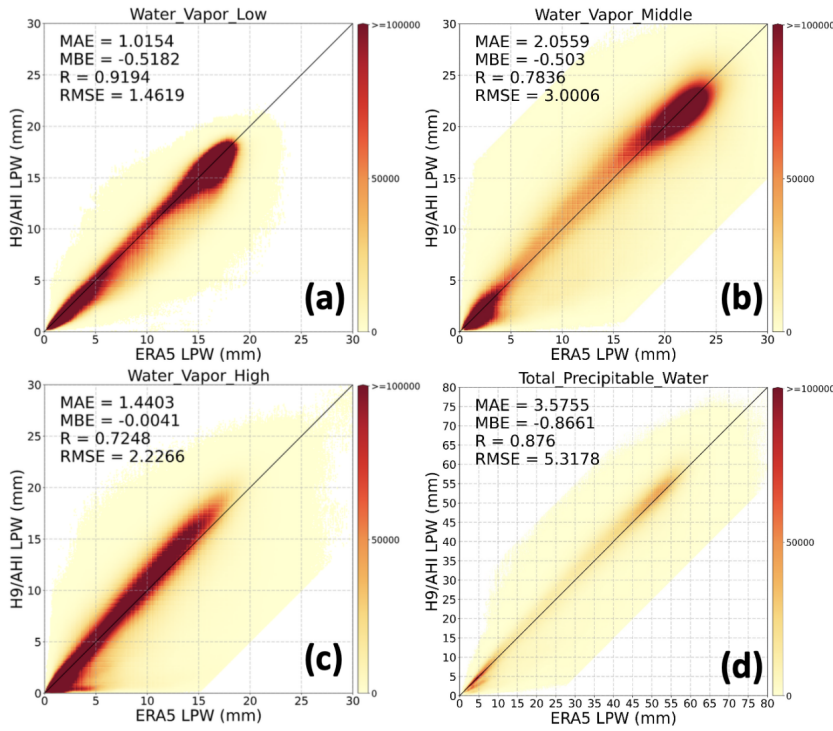
1158 **Figure 7.** ERA5 (first column panel) and H9/AHI GEO satellite (middle column panel)
 1159 atmospheric (a, e) water vapor at low layer (Surface-900hPa), (b, f) water vapor at
 1160 middle layer (900-700hPa), (c, g) water vapor at high layer (700-300hPa), (d, h) total
 1161 precipitable water, (i) H9/AHI CAPE index, (j) H9/AHI K index, (k) H9/AHI LI index,
 1162 and (l) H9/AHI Showalter index at 09:00 UTC on January 4, 2023 over the
 1163 NANO_SCS system.

1164

1165

删除了: SCS

1167



1168

1169 **Figure 8.** Comparisons of the [one year \(2023\)](#) layered precipitable water (LPW) values
 1170 (a, Low; b, Middle; c, High; d, Total) from ERA5 reanalysis and H9/AHI data over the
 1171 [NANO SCS system](#). The color bar represents the total number in every bin at an
 1172 interval of 0.1 mm.

1173

1174

1175

1176

1177

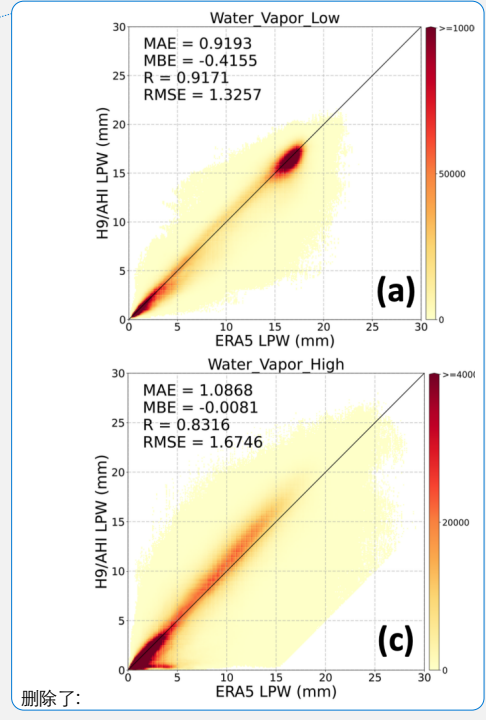
1178

1179

1180

1181

1182



删除了:

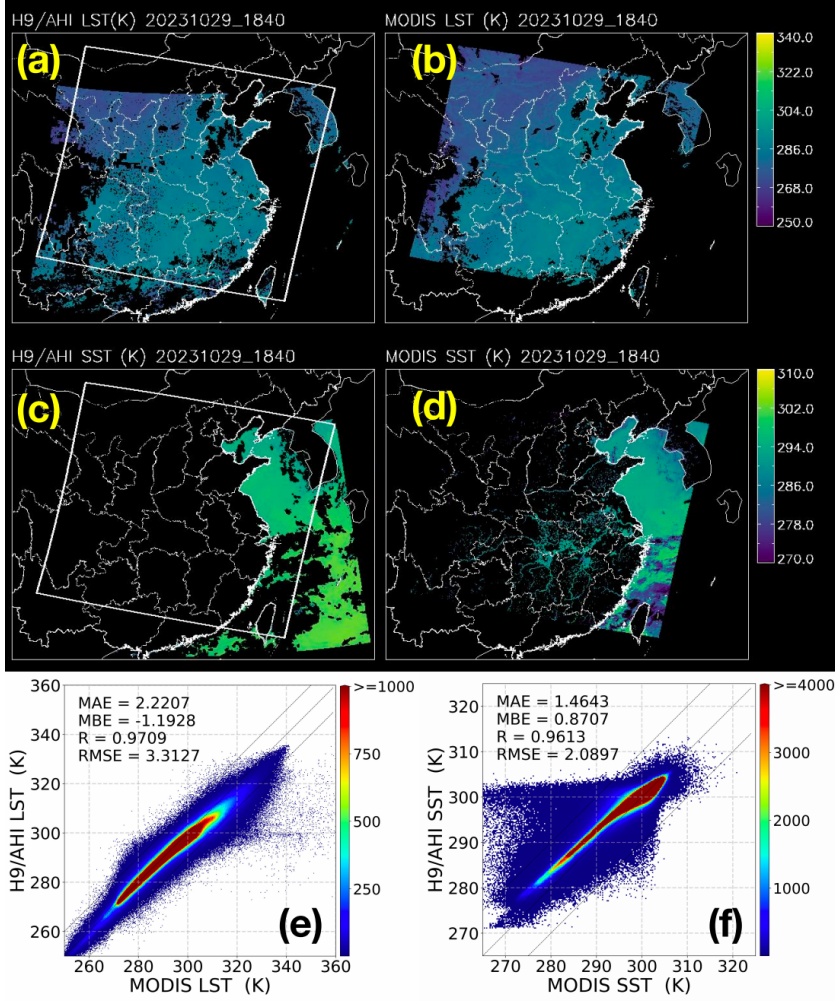
删除了: four months

删除了: January, April, July, and October of

删除了: SCS

删除了: ←

1188
1189



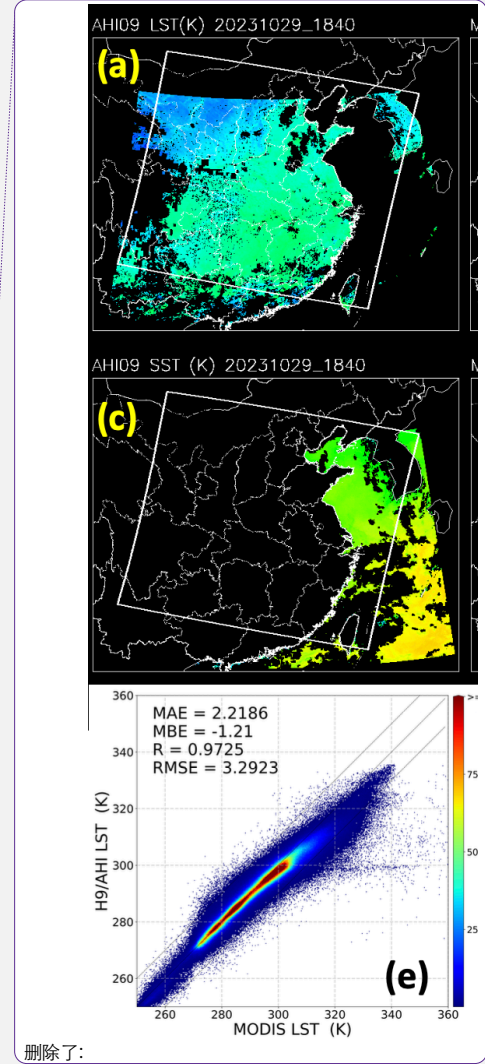
1190

1191 **Figure 9.** LST (top panel) and SST (middle panel) comparisons between (a, c) H9/AHI
 1192 GEO satellite and (b, d) MODIS at 18:40 UTC on October 29, 2023. Comparisons of
 1193 the one year (2023) (e) LST and (f) SST from MODIS and H9/AHI data over the
 1194 NANO_SCS system. The color bar represents the total number in every bin at an
 1195 interval of 0.25 K of LST or SST.

1196

1197

删除了: ←



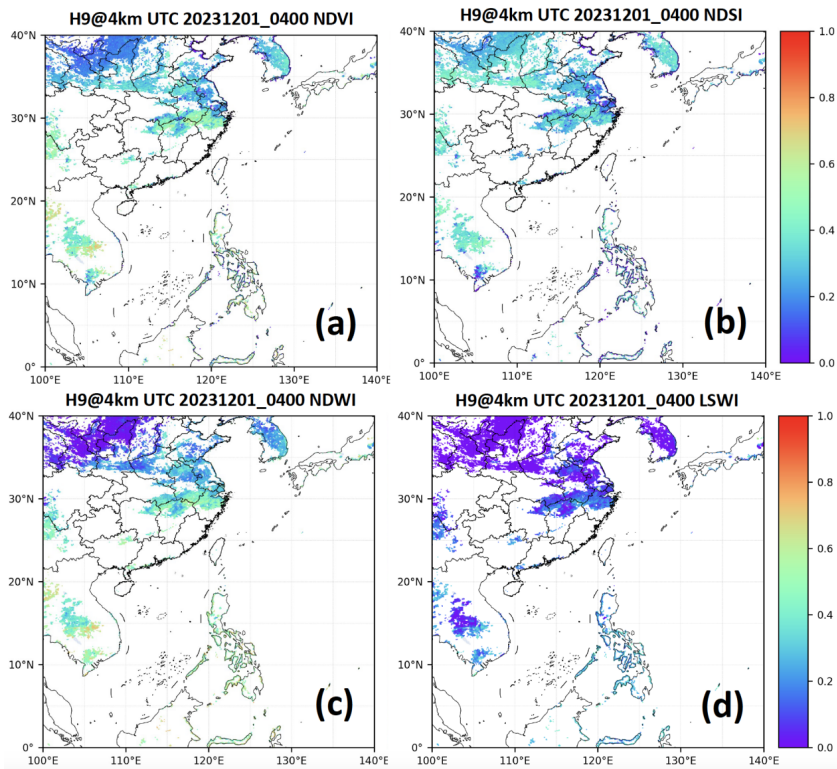
删除了:

删除了: four months

删除了: January, April, July, and October of

删除了: SCS

1204
1205



1206
1207 **Figure 10.** (a) NDVI, (b) NDSI, (c) NDWI, and (d) LSWI maps retrieved by H9/AHI
1208 at 04:00 UTC on December 1, 2023 over the NANO_SCS system,
1209

删除了: SCS